Linear-Chain Structure in Carbon Isotopes
炭素同位体における直鎖クラスター構造

Tomoyuki Baba

Department of Cosmosciences
Graduated School of Science
Hokkaido University

March, 2019

Abstract

To establish the existence of the linear-chain structure, we theoretically investigate excited states in ^{14}C and ^{16}C by using the antisymmetrized molecular dynamics. For ^{14}C, it is found that two types of linear-chain formation, π-bond and σ-bond linear chains, appear in positive-parity states. The calculated excitation energies, moments of inertia, and α-decay widths of the linear-chain states are compared with the observed data reported by recent experiments. The properties of the π-bond linear-chain states reasonably agree with the observation, which convinces us of the linear-chain formation in ^{14}C. In addition, we suggest characteristic decay patterns and Coulomb shifts as the way to distinguish the π-bond and σ-bond linear chains. As a result, the σ-bond linear chain is a good candidate for the higher-lying resonant states reported by a cluster-transfer experiment. For ^{16}C, it is found that the positive-parity linear-chain states have the $(3/2^-_\pi)^2(1/2^-_\sigma)^2$ configuration and primary decay to ^{12}Be(2^+_1) as well as to ^{12}Be(g.s.) by α-particle emission. Moreover, we show that they also decay via the ^{6}He + ^{10}Be channel. In the negative-parity states, it is found that two types of the linear chains exist. One has the valence neutrons occupying the molecular orbits $(3/2^-_\pi)^2(1/2^-_\sigma)(3/2^+_\pi)$, while another configuration cannot be explained in terms of the molecular orbits because of the strong parity mixing. Their α and ^{6}He reduced widths are sufficiently large to be distinguished from other non-cluster states although they are smaller than those of the positive-parity linear chain.

Contents

Chapter 1

Introduction

1.1 Nuclear Clusters

The atomic nucleus is a many-body system of strongly interacting protons and neutrons. To describe this complicated system, there are many models. The shell model, treating the motion of the nucleons as independent particles moving in a mean-field potential, leads to the most notable success which explains the magic numbers [1]. In contrast to this "atom-like" picture, the excited states of light nuclei show the α cluster structure composed of weak interacting α-particles (formed from two protons and two neutrons, that is, ^{4}He nucleus), which is regarded as the "molecule-like" picture (see Fig. 1.1). Because the binding energy of the α-particle is much larger than those of other light nuclei, it is likely to form the subsystem in a nucleus.

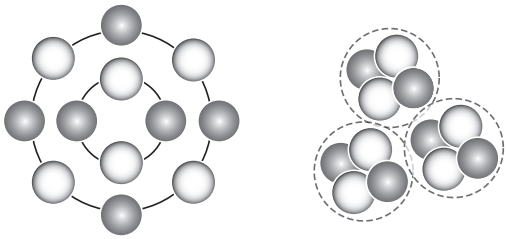

Figure 1.1: Schematic illustration of shell structure(left) and cluster structure(right)

Such clustering and molecular states in atomic nuclei were predicted in 1930s [2], and were reviewed in 1960s because of two reasons. The first reason is the Hoyle state. To explain the abundance of carbon, Hoyle predicted the existence of the resonance state composed of three α-particles around the $\alpha+\alpha+\alpha$ threshold to which ^{12}C decays [3]. Such a state at an excitation energy 7.654 MeV was experimentally confirmed soon afterwards [4]. Therefore, this second 0^+ state is well-known as the Hoyle state and plays a important role in stellar nucleosynthesis. However, it is not easy to describe this state by using the shell model with harmonic oscillator basis [5]. On the other hand, several cluster models have challenged and succeeded to reproduce the excitation spectrum of ^{12}C, especially the 0^+_2 state [6–9]. It has been pointed out that the Hoyle state can be viewed as a dilute gas of weakly interacting α-particles which is analogous to the properties of a Bose-Einstein condensation [10–12]. Today, it still attracts much interest and is investigated by many theoretical [13–16] and experimental [17–19] studies.

The second reason is the first excited state of ^{16}O. This first excited 0^+ state at 6.05 MeV was not understood by the simple shell model, and hence, it was called as the "mysterious 0^+ state". A number of works [20–23] have been discussed this state, and at present, it is found that the 0^+_2 state is the asymmetric cluster structure composed of $\alpha + ^{12}$C clusters. While the 0^+_2 state is interpreted that the α-particle goes around the ^{12}C(0^+) core with s-wave (notated as $[^{12}\mathrm{C}(0^+) \otimes l = 0]_{J=0}$), the 0^+_3 state at 12.05 MeV is interpreted that the α-particle goes around the ^{12}C(2^+) core with d-wave ($[^{12}\mathrm{C}(2^+) \otimes l = 2]_{J=0}$). Moreover, such asymmetric cluster structure forms the two rotational bands with positive parity ($K = 0^+$) and negative parity ($K = 0^-$), which is well-known as the

inversion doublet. The inversion doublet is the most prominent signature as the asymmetric cluster formation and has been observed in not only ^{16}O but also ^{20}Ne ($\alpha + {}^{16}$O) and ^{44}Ti ($\alpha + {}^{40}$Ca) by many experiments [24].

In addition to the cluster structures as mentioned above, many different types of cluster structure appear as the excitation energy increases [25–28]. Figure 1.2, called as the Ikeda diagrams [29], displays various cluster structures in terms of nuclei with an equal and even number of protons and neutrons ($Z = N$). As shown in this figure, cluster structures are predicted to appear as excited states close to the corresponding decay threshold, which is known as the threshold rule. The threshold rule provides us with an important view to understand the clustering. However, the detailed mechanism of the cluster formation has not been understood completely. To shed some light on the clustering, we focus on the linear-chain structure which is one of the most interesting and exotic cluster formation. Such a configuration composed of linearly aligned three α-particles was for the first time suggested by Morinaga [30]. It has a 3:1 ratio of the large axis over the small axis, so-called hyper-deformation, and such extremely deformed nuclei have not yet been observed. Therefore, the linear-chain structure can provide us with an understanding of not only the nature of the cluster formation but also the extreme deformation of nuclear shape. For the above reasons, the linear-chain structure has long been an important subject of the nuclear physics.

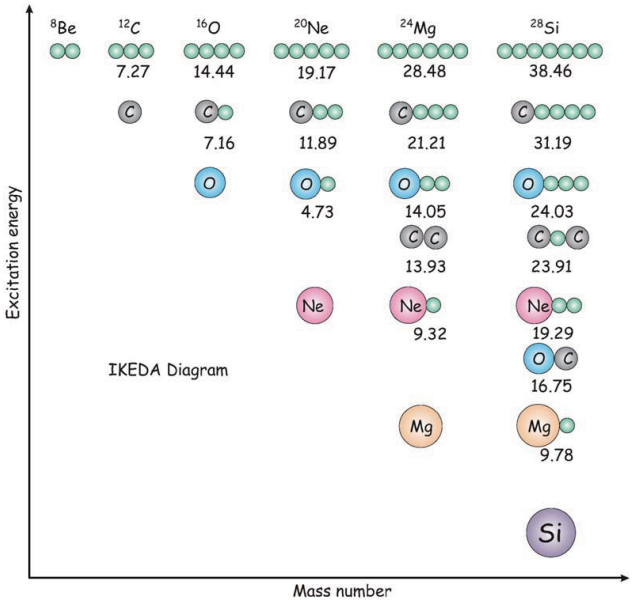

Figure 1.2: Threshold rule shown by Ikeda diagram [29, 38].

The 0_2^+ state in ^{12}C was the first candidate for the linear-chain state. As mentioned above, however, it turned out that it does not have the linear-chain configuration but are loosely coupled 3α clusters with dilute gas-like nature [10]. Sequentially, although the 0_3^+ state at 10.3 MeV in ^{12}C was suggested as the linear-chain state, recent studies [16,31,32] have pointed out that the 0_3^+ state in ^{12}C appears as a family state of the Hoyle state to have a higher nodal structure in the internal motions of the 3α clusters. Alternatively, the 0_4^+ state in ^{12}C has been suggested for the candidate for the linear-chain state [16]. For ^{12}C, however, the instability of the linear-chain configuration against the bending motion (deviation from linear alignment) was pointed out and the bent-armed configuration was predicted by the antisymmetrized molecular dynamics (AMD) [13, 33, 34] and Fermionic molecular dynamics (FMD) calculations [12, 35]. This reason is explained as followings. When aligned three α-particles in z-axis linearly, the eight nucleons composing of the two α-particles must be excited with respect to principal quantum number of z-axis, n_z, and occupy the higher orbits because of the Pauli blocking. Bending the linear chain, one α-particle can be de-excited and gain the less potential energy. Therefore, the bent-armed linear-chain configuration is more stable than the ideal linear-chain configuration for ^{12}C. Furthermore, a rotational band of ^{16}O has been observed around the 4α threshold with a very large moment of inertia [36], and hence, the existence of the 4α linear chain has been discussed [37]. However, it is not clearly been confirmed in experiments.

1.2 Molecular Orbit

A renewed interest in neutron-rich nuclei again led to the studies on the linear-chain structure because extra neutrons may stabilize unstable cluster structure such as the linear-chain configuration [38]. Various types of the cluster structure composed of α and ^{16}O core with several neutrons are shown in Fig. 1.3 which was suggested as the extended Ikeda diagrams. This stabilization mechanism is well known for Be isotopes in which 2α cluster core [39–45]. For example, ^{8}Be is a unstable nucleus for an α-emission although it has a developed cluster structure. Adding one and two valence neutrons, ^{9}Be and ^{10}Be become stable and they are famous examples of the clustering. Therefore, the role of valence neutrons can be interpreted as the "glue-like" effect and it is analogous to the covalent bond in the molecule. Furthermore, it has been suggested that more neutron-rich isotopes ^{11}Be and ^{12}Be have more developed cluster structure than ^{10}Be [46, 47]. This fact is also confirmed by the observations of the increase of the proton radii [48,49]. Thus, the role of valence neutrons is not only the bonding but also the development for clusters.

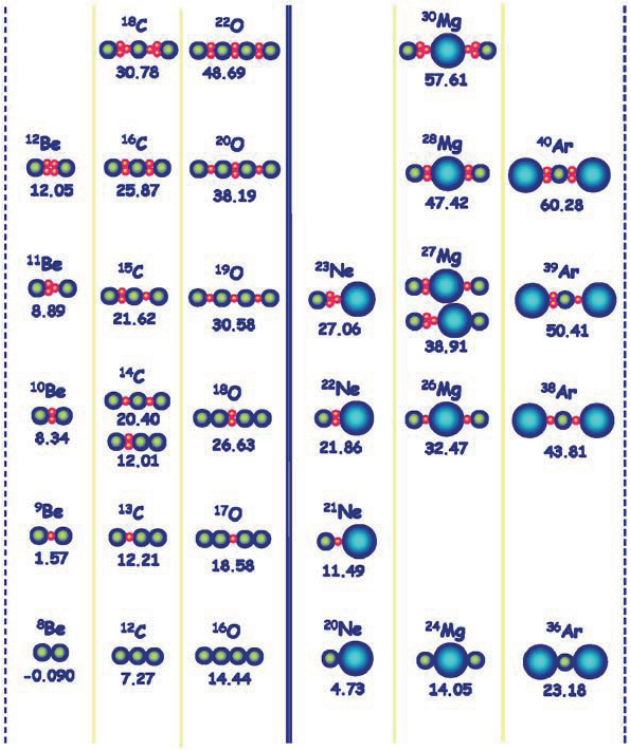

Figure 1.3: Extended Ikeda diagram suggested by W. von Oertzen *et al.* [38].

These roles are explained by the molecular orbits formed around the 2α core shown in Figure 1.4. Molecular orbits are composed of the linear combination of p-wave around the core and classified into two types; π-orbit which is perpendicular to the symmetry axis of 2α core and σ-orbit which is parallel to the symmetry axis. In the case of ^{10}Be, it is found that the two valence neutrons of the ground state 0^+_1 occupy the π-orbit, on the other hand, those of the 0^+_2 state at 6.18 MeV occupy the σ-orbit. The π-orbit stabilizes the cluster structure and shortens the distance of the 2α core, whereas the σ-orbit develops the cluster structure and elongates the distance of the 2α core. Hence, ^{9}Be and ^{10}Be become more stable than ^{8}Be occupying one and two neutrons in the π-orbit, and ^{11}Be and ^{12}Be develop the cluster than ^{9}Be and ^{10}Be occupying additional one and two neutrons in the σ-orbit. Incidentally, it was suggested by the generalized two-center cluster model [50] that as the excitation energy in ^{12}Be increases various "ionic" configurations such as $\alpha + {}^{8}$He, ^{6}He + ^{6}He, and ^{5}He + ^{7}He appear as the molecular resonances. It is also interesting phenomena as an analogy to the molecular structure.

As a natural consequence, it is expected that the linear-chain configuration can be realized in neutron-rich C isotopes owing to the molecular orbits of valence neutrons (Fig. 1.5) instead of the $N = Z$ nucleus, ^{12}C. This expectation has motivated many theoretical studies [51–61]. Itagaki *et al.* [51] investigated the stability against the breathing and bending modes with respect to the linear-chain configuration of the carbon isotopes ($A = 12, 14, 16$) based on the molecular orbital model. As the result, it is found that the linear-chain state of ^{16}C with the $\pi^2\sigma^2$ configuration for the four valence neutrons is the most promising candidate among carbon isotopes. Figure 1.6 shows that the only ^{16}C($\pi^2\sigma^2$) configuration has the minimum at the bending angle $\theta = 0$, which means the stability against the bending motion. Although this previous work used the microscopic model assuming 3α cluster core, π and σ molecular orbits of valence neutrons, it attracted considerably renewed interest

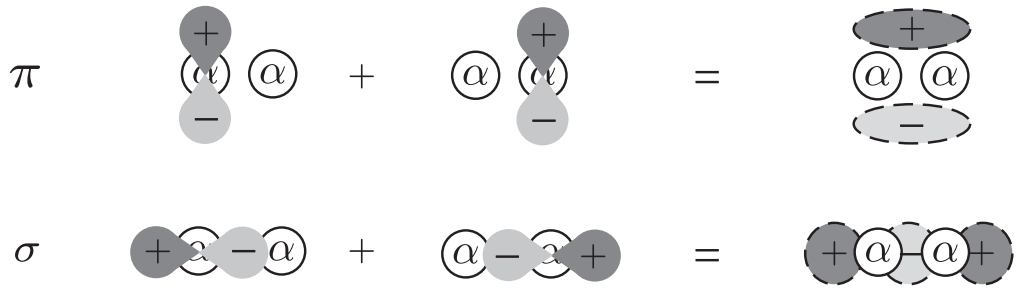

Figure 1.4: Schematic illustration of the π-orbit (top) and σ-orbit (bottom) in the 2α system. They are described by the linear combination of p-wave at the α core.

in the linear-chain structure in neutron-rich nuclei. Suhara *et al.* [55] searched for excited states in ^{14}C using a method of antisymmetrized molecular dynamics (AMD) in combination with the generator coordinate method (GCM). They found that the linear-chain band in positive-parity states, here, the valence neutrons occupy the π-orbit located around two of the three α clusters, namely, the $\alpha + {}^{10}\mathrm{Be}(\pi^2)$. They in detail studied the origin of this asymmetric $\alpha + {}^{10}$Be correlation and indicated that this configuration has its origin in the many-body correlation incorporated by the parity projection [56].

1.3 Experimental Results for Linear-Chain States

Although many theoretical calculations predicted the existence of the linear-chain configuration, it had not been clearly observed by a number of experiments in 2000s [62–68]. However, recent years have seen several important experimental studies for the linear-chain states in ^{14}C [69–73]. Rather promising candidates of the π-bond linear-chain configuration in ^{14}C were independently reported by three groups [69–71]. These groups observed the $\alpha + {}^{10}$Be resonances above the α threshold energy in both of positive and negative parity. In particular, Yamaguchi *et al.* [71] updated the information about the candidates of the π-bond linear chain. Although the spin-parity assignments for several states are not consistent with those found in previous experiments [67, 69, 70], they firstly observed a candidate for the band-head of the linear-chain ($J^\pi = 0^+$) at 15.07 MeV, which should be compared with the theoretical calculations. Owing to the better statistics and larger angular coverage, they provided more reliable spin-parity assignment and evaluation of the decay widths. Figure 1.7 shows that the reported energies of the positive-parity resonances measured from the α threshold are in reasonable agreement with the excitation energies of the linear-chain states predicted by Suhara *et al.* [55]. Thus, rather promising evidence of the π-bond linear-chain formation has been found.

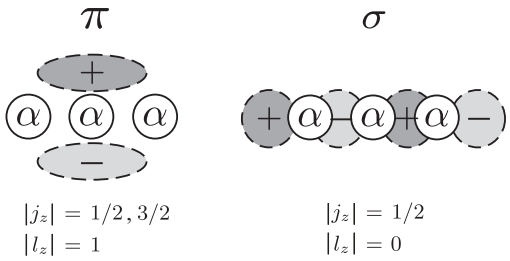

Figure 1.5: Schematic illustration of the π-orbit (left) and σ-orbit (right) in the 3α system. The parity of the σ-orbit is different from that of 2α system

Quite recently, very interesting data were reported by two works Tian *et al.* [72] and Li *et al.* [73]. They reported the resonances populated by ^{9}Be(^{9}Be, $\alpha + {}^{10}$Be)α reaction. In addition to the same resonances reported by $\alpha + {}^{10}$Be elastic scattering, they reported the decay properties of two resonances located *above* the $\alpha + {}^{10}$Be and $2\alpha + {}^{6}$He thresholds, which are shown as the light-blue lines and the relative branching ratio in Fig. 1.7. The relative branching ratio of the lower resonance at 21.4 MeV shows that the decay into the π-orbit of ^{10}Be(2^+) is dominant. Therefore,

this resonance is a good candidate for the π-bond linear-chain state. On the other hand, the relative branching ratio of the higher resonance at 22.5 MeV shows that the decay into the 6 MeV state of ^{10}Be is dominant. Given that this ^{10}Be state locates near the 0_2^+ state at 6.18 MeV, the higher resonance dominantly decays into the σ-orbit of ^{10}Be. Therefore, based on this very interesting decay pattern, this new resonance was suggested as the candidates of the σ-bond linear chain.

A high-lying excited state at 20.6 MeV in ^{16}C was observed by the breakup of ^{6}He + ^{10}Be [74]. Although further experimental studies are needed, given that the higher resonances in ^{14}C are good candidates of the linear-chain states, it is expected that the observed high-lying state can be also the candidate for the linear-chain state in ^{16}C.

1.4 Purpose

Although the reported energies in Refs. [69–71] and the predicted excitation energies in Ref. [55] are close to each other, there are still several gaps between theory and experiment which must be resolved to confirm the linear-chain formation in ^{14}C. First, when measured from the ground state energy, theoretically predicted and experimentally observed excitation energies of the positive-parity resonances disagree. This may be because the effective interaction used in the calculation [75] do not reproduce the α threshold energy. Second, the experiments report the negative-parity resonances, while the negative-parity linear-chain states were not clearly identified in Ref. [55].

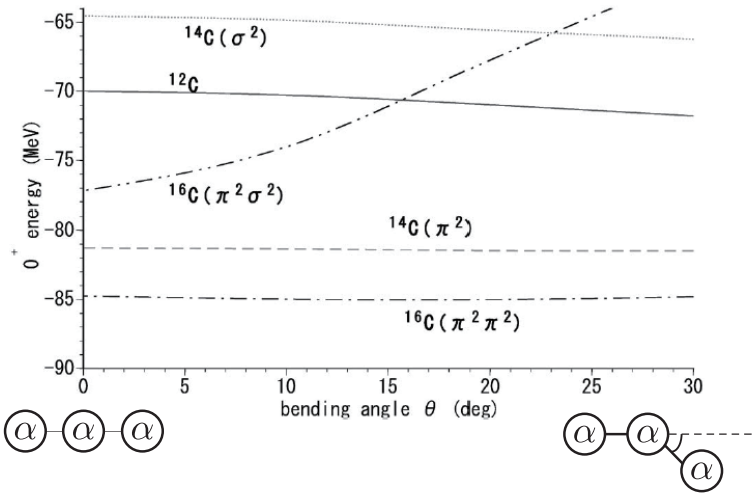

Figure 1.6: The 0^+ energy curves against the bending angle θ for carbon isotopes [51].

Third, the experiments reported the α-decay width of the resonances which is a strong evidence of the α clustering and must be verified by the theoretical calculation. Thus, further theoretical studies are in need to identify the linear-chain states in ^{14}C. Finally, the observed unique decay patterns of the resonances reported by Tian *et al.* [72] and Li *et al.* [73] suggested the possibility of the existence of the σ-bond linear-chain state. However, it has not been discussed in carbon isotopes although the σ-orbit of beryllium isotopes is well known. Also, we are interested in how to distinguish the σ-bond linear chain from the π-bond linear chain, especially their decay patterns.

^{16}C is also very interesting nucleus as the most promising candidate for the stable linear-chain state, because its stability against the bending motion was pointed out by molecular orbital model calculation [51]. Because this previous work assumed the 3α cluster core and molecular orbits of valence neutrons, it is very important to investigate the linear-chain state in ^{16}C without any *a priori* assumptions on the cluster core and valence neutron orbits. Furthermore, in addition to the linear-chain configuration, triangular configurations of three α-particles are also suggested in the neighboring nuclei such as ^{13}C and ^{14}C [55, 58, 76]. Therefore, it is also interesting to search for analogous state in ^{16}C. For further experimental study, we provide additional theoretical informations. The first is negative-parity states. In the case of ^{14}C, the experiments have reported the negative-parity resonances [69–71]. Therefore, theoretical predictions are also needed for the negative-parity resonances in ^{16}C. The second is decay mode of the linear-chain configuration. If

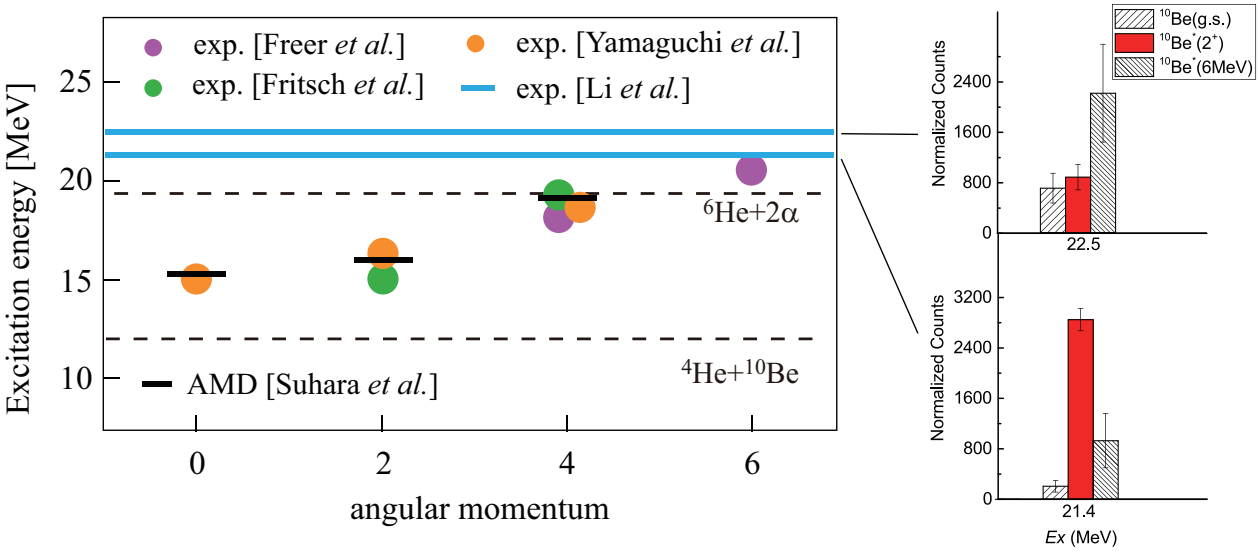

Figure 1.7: Left: Excitation spectra of the experiments [69–71, 73] and the calculation [55] in ^{14}C. Dashed lines show the experimental $\alpha + {}^{10}$Be and ^{6}He+2α thresholds. Right: Observed relative branching ratio for two resonances with respect to three sets of final states in ^{10}Be [73].

the linear-chain states of ^{16}C are predicted above the $\alpha + {}^{12}$Be and ^{6}He$+{}^{10}$Be thresholds, the decay pattern should provide important information to identify the linear-chain configuration.

For these purposes, we investigate the linear-chain states in ^{14}C and ^{16}C by using the method of AMD. For the sake of the quantitative comparison of the excitation energy, we employ Gogny D1S effective interaction [77] which reproduces threshold energies in ^{14}C. From the AMD wave function, we estimate the α-decay widths of the linear-chain states as well as those of other cluster and non-cluster states. It is found that the calculated excitation energies of the π-bond linear-chain states in positive parity are in good agreement with the observation, and only the linear-chain states have large α-decay widths comparable with the observed data. Hence, we consider that the π-bond linear-chain formation in the positive-parity state is rather plausible. On the other hand, in the negative-parity state, the linear-chain configuration does not correspond to a single eigenstate but is mixed with other configurations in the eigenstates. Thus, the linear-chain configuration does not form a single rotational band. As a further evidence of the linear-chain formation, we focus on the α-decay pattern. It is shown that the linear-chain states decay to the excited states of ^{10}Be as well as the ^{10}Be ground state, while other cluster states dominantly decay to the ^{10}Be ground state. In addition to these analysis, it is found that the σ-bond linear chain decays to the ^{6}He$+{}^{8}$Be channel as well as the $\alpha + {}^{10}$Be(σ^2) channel, and their branching ratios are comparable. Hence, we suggest that the sequential three-body decay of ^{14}C$^* \to {}^{6}$He$+{}^{8}$Be $\to {}^{6}$He$+\alpha+\alpha$ is an important evidence of the σ-bond linear chain. These characteristic decay patterns are, if it is observed, a strong signature of the linear-chain formation. We also focus on the Coulomb shift of the σ-bond linear chain in the mirror pair of ^{14}C and ^{14}O.

In the case of ^{16}C, we study the positive- and negative-parity linear-chain states and discuss their decay patterns. The positive-parity linear-chain has the valence neutrons occupying molecular orbits $(3/2^-_\pi)^2(1/2^-_\sigma)^2$. We predict that the linear-chain states primarily decay to ^{12}Be(2^+_1) as well as to ^{12}Be(g.s.). They will also decay to ^{10}Be(g.s.) and ^{10}Be(2^+_1) by ^{6}He emission, which is a signature of the covalency of valence neutrons. In the negative parity, two rotational bands composed of

the linear-chain configuration are found. One has the valence neutrons occupying the molecular orbits $(3/2^-_\pi)^2(1/2^-_\sigma)(3/2^+_\pi)$, and the other does not have the clear molecular orbital configuration. Their α- and ^{6}He reduced widths are smaller than those of positive-parity linear-chain band, but sufficiently large to be distinguished from other non-cluster states.

This paper is organized as follows. In Chapter 2, we explain the AMD framework which has the advantage to describe the nuclear structure without any *a priori* assumptions. In Section 2.5, we give the method to estimate the reduced widths amplitude for the $\alpha + {}^{10,12}$Be and $^6\mathrm{He} + {}^{8,10}$Be decays in order to compare the α-decay widths with the observations and discuss characteristic decay patterns of the linear-chain configuration. In Section 3.1, the excitation energies and decay widths of the linear-chain states in ^{14}C are shown and compared with the observed data to suggest the assignment of the linear-chain bands. In addition, in order to show the further signature for the σ-bond linear chain, the Coulomb shifts in the mirror pair of ^{14}C and ^{14}O are discussed in Subsection 3.1.6. In the same manner, the results for ^{16}C are also discussed in Section 3.2. In Chapter 4, we summarize these works.

Chapter 2

Theoretical Framework

In this work, using the intrinsic AMD wave function and effective interaction shown in Section 2.1, we perform the variational calculation shown in Section 2.2. Obtained wave functions are not eigenstates of angular momentum so that the angular momentum projection is also needed. To obtain the precise eigenenergy and eigenfunction, we perform the generator coordinate method (GCM) shown in Section 2.3. In addition, using the wave function obtained by GCM, we calculate the single-particle properties which are useful to check the properties of molecular orbits in Section 2.4. Finally, we mention the methods to estimate the reduced width amplitude using the two ways, the approximated method and the Laplace expansion method, shown in Section 2.5. Main efforts by the AMD calculation are reviewed in these Refs. [78, 79].

2.1 AMD Wave Function and Effective Hamiltonian

In this work the microscopic A-body Hamiltonian is written as

$$\hat{H} = \sum_{i=1}^{A} \hat{t}_i - \hat{t}_{c.m.} + \sum_{i<j}^{A} \hat{v}_{ij}^{N} + \sum_{i<j}^{Z} \hat{v}_{ij}^{C}, \tag{2.1}$$

where $\hat{t}_i$, $\hat{t}_{c.m.}$, $\hat{v}^N$, and $\hat{v}^C$ are the kinetic energy per nucleon, kinetic energy of the center-of-mass, nucleon-nucleon interaction and Coulomb interaction, respectively. The Coulomb interaction $\hat{v}^C$ is approximated by a sum of seven Gaussians. The Gogny D1S [77] is used as the effective nucleon-nucleon interaction,

$$\begin{aligned}\hat{v}_{ij}^{NN} = &\sum_{j=1}^{2} \exp\left(-\frac{(\mathbf{r}_1-\mathbf{r}_2)^2}{\mu_j^2}\right)(W_j + B_j\hat{P}_\sigma - H_j\hat{P}_\tau - M_j\hat{P}_\sigma\hat{P}_\tau) \\ &+iW_{LS}\overleftarrow{\nabla}_{12}\delta(\mathbf{r}_1-\mathbf{r}_2)\times\overrightarrow{\nabla}_{12}\cdot(\sigma_1+\sigma_2) \\ &+t_3(1+x_0\hat{P}_\sigma)\delta(\mathbf{r}_1-\mathbf{r}_2)\left[\rho\left(\frac{\mathbf{r}_1+\mathbf{r}_2}{2}\right)\right]^{\alpha},\end{aligned} \tag{2.2}$$

where each term is central force, spin-orbit force, and density-dependent force in order. This interaction depends on 14 parameters which are adjusted fitting sets of nuclear matter and finite nuclear properties. The Gogny D1S parameters were modified from the Gogny D1 parameters [80] to reproduce the barrier heights in actinides. At present, the D1S interaction has been used to describe phenomena such as giant resonances, shape coexistence, super-deformation and fission fragment properties. It is shown that the Gogny D1S interaction reasonably describes the n-, α-, and ^{6}He-threshold energies within 1 MeV error.

The AMD wave function $\Phi_{\rm AMD}$ is represented by a Slater determinant of single-particle wave packets,

$$\Phi_{\rm AMD} = \mathcal{A}\{\varphi_1, \varphi_2, ..., \varphi_A\} = \frac{1}{\sqrt{A!}}\det[\varphi_i(\mathbf{r}_j)] = \frac{1}{\sqrt{A!}}\begin{vmatrix} \varphi_1(\mathbf{r}_1) & \varphi_1(\mathbf{r}_2) & \dots & \varphi_1(\mathbf{r}_A) \\ \varphi_2(\mathbf{r}_1) & \varphi_2(\mathbf{r}_2) & \dots & \varphi_2(\mathbf{r}_A) \\ \vdots & \vdots & \ddots & \vdots \\ \varphi_A(\mathbf{r}_1) & \varphi_A(\mathbf{r}_2) & \dots & \varphi_A(\mathbf{r}_A) \end{vmatrix}, \quad (2.3)$$

where φ_i is the single-particle wave packet which is a direct product of the deformed Gaussian spatial part [81], spin (χ_i) and isospin (ξ_i) parts,

$$\begin{aligned} \varphi_i(\mathbf{r}) &= \phi_i(\mathbf{r}) \otimes \chi_i \otimes \xi_i, & (2.4)\\ \phi_i(\mathbf{r}) &= \prod_{\sigma=x,y,z}\Big(\frac{2\nu_\sigma}{\pi}\Big)^{1/4}\exp\Big\{-\nu_\sigma\Big(r_\sigma - \frac{Z_{i\sigma}}{\sqrt{\nu_\sigma}}\Big)^2\Big\}, & (2.5)\\ \chi_i &= a_i|\uparrow\rangle + b_i|\downarrow\rangle, \quad |a_i|^2 + |b_i|^2 = 1, & (2.6)\\ \xi_i &= \text{proton or neutron} & (2.7) \end{aligned}$$

The centroids of the Gaussian wave packets $\mathbf{Z_i}$, the direction of nucleon spin a_i, b_i, and the width parameter of the deformed Gaussian ν_σ are the variables determined by the frictional cooling method explained below. It is noted that the AMD wave function Eq. (2.3) can be analytically decomposed into the internal wave function Φ_{int} and the center-of-mass wave function $\Phi_{c.m.}$,

$$\begin{aligned} \Phi_{\rm AMD} &= \Phi_{int}\Phi_{c.m.}, & (2.8)\\ \Phi_{c.m.} &= \prod_{\sigma=x,y,z}\Big(\frac{2A\nu_\sigma}{\pi}\Big)^{1/4}\exp\{-A\nu_\sigma R_\sigma^2\}, & (2.9)\\ R_\sigma &= \frac{1}{A}\sum_{i=1}^{A} r_{i\sigma}. & (2.10) \end{aligned}$$

Therefore, the center-of-mass kinetic energy $\hat{t}_{c.m.}$ in Eq. (2.1) is exactly removed and the model is free from the spurious motion.

The intrinsic wave function is projected to the eigenstate of the parity to investigate both of the positive- and negative-parity states,

$$\Phi^\Pi = \hat{P}^\Pi\Phi_{int} = \frac{1+\Pi\hat{P}_x}{2}\Phi_{int}, \quad \Pi = \pm, \quad (2.11)$$

where $\hat{P}^\Pi$ and $\hat{P}_x$ denote a parity projector and the parity operator, that is,

$$\hat{P}_x\phi_i(\mathbf{r}) = \phi_i(-\mathbf{r}). \quad (2.12)$$

2.2 Variation and Angular Momentum Projection

The variational energy is defined as,

$$E^\Pi = \frac{\langle\Phi^\Pi|H|\Phi^\Pi\rangle}{\langle\Phi^\Pi|\Phi^\Pi\rangle} \quad (2.13)$$

By the frictional cooling method [82], the variables of the wave function ($\mathbf{Z_i}$, a_i, b_i, ν_σ) are determined so that E^Π is minimized. To obtain the large deformed states, in this study, we add the constraint potential to the variational energy,

$$\tilde{E}^\Pi = \frac{\langle\Phi^\Pi|H|\Phi^\Pi\rangle}{\langle\Phi^\Pi|\Phi^\Pi\rangle} + v_\beta(\langle\beta\rangle - \beta)^2 + v_\gamma(\langle\gamma\rangle - \gamma)^2, \quad (2.14)$$

where $\langle\beta\rangle$ and $\langle\gamma\rangle$ are the quadrupole deformation parameters of the intrinsic wave function defined in Ref. [55],

$$\langle x^2\rangle = R_0^2\Big\{1+\sqrt{\frac{5}{4\pi}}\beta\cos(\gamma+\frac{2\pi}{3})\Big\}, \tag{2.15}$$

$$\langle y^2\rangle = R_0^2\Big\{1+\sqrt{\frac{5}{4\pi}}\beta\cos(\gamma-\frac{2\pi}{3})\Big\}, \tag{2.16}$$

$$\langle z^2\rangle = R_0^2\Big\{1+\sqrt{\frac{5}{4\pi}}\beta\cos(\gamma)\Big\}, \tag{2.17}$$

$$R_0^2=\frac{1}{3}(\langle x^2\rangle+\langle y^2\rangle+\langle z^2\rangle),\quad \langle z^2\rangle\geq\langle y^2\rangle\geq\langle x^2\rangle. \tag{2.18}$$

Here, $\langle x^2\rangle=\langle\Phi^\pi|x^2|\Phi^\pi\rangle$ (y and z are also same.). The v_β and v_γ parameters are chosen to be large enough that $\langle\beta\rangle$ and $\langle\gamma\rangle$ are equal to β and γ after the variation.

The variables are determined based on the imaginary-time evolution equation,

$$\frac{dX_i}{dt}=-\frac{\mu}{\hbar}\frac{\partial E}{\partial X_i^*}, \tag{2.19}$$

where μ is the positive constant and X_i is the variables $\mathbf{Z_i}$, a_i, b_i, ν_σ. Using this equation, the total energy always decreases as follows:

$$\begin{aligned}\frac{dE}{dt} &= \sum_i\left(\frac{\partial E}{\partial X_i}\frac{dX_i}{dt}+\frac{\partial E}{\partial X_i^*}\frac{dX_i^*}{dt}\right)=-\frac{\mu}{\hbar}\sum_i\left(\frac{\partial E}{\partial X_i}\frac{\partial E}{\partial X_i^*}+\frac{\partial E}{\partial X_i^*}\frac{\partial E}{\partial X_i}\right)\\ &= -\frac{2\mu}{\hbar}\sum_i\left|\frac{\partial E}{\partial X_i}\right|^2\leq 0.\end{aligned} \tag{2.20}$$

By minimizing $\tilde{E}^\Pi$, we obtain the optimized wave function $\Phi^\Pi(\beta,\gamma)=\hat{P}^\Pi\Phi_{int}(\beta,\gamma)$ which has the minimum energy for each set of β and γ.

Because the wave functions obtained by the variational calculation are not eigenstates of angular momentum, the eigenstate of the total angular momentum J is projected [83] out from $\Phi^\Pi(\beta,\gamma)$,

$$\Phi^{J\pi}_{MK\beta_i\gamma_i}=\frac{\hat{P}^J_{MK}\Phi^\pi_{\beta_i\gamma_i}}{\sqrt{\langle\hat{P}^J_{MK}\Phi^\pi_{\beta_i\gamma_i}|\hat{P}^J_{MK}\Phi^\pi_{\beta_i\gamma_i}\rangle}}. \tag{2.21}$$

$\hat{P}^J_{MK}$ is the angular momentum projector,

$$\hat{P}^J_{MK}=\frac{2J+1}{8\pi^2}\int d\Omega D^{J*}_{MK}(\Omega)\hat{R}(\Omega), \tag{2.22}$$

where $D^J_{MK}(\Omega)$ and $\hat{R}(\Omega)$ are the Wigner D function and the rotation operator,

$$D^J_{MK}(\Omega) = \langle JM|\hat{R}(\Omega)|JK\rangle, \tag{2.23}$$

$$\hat{R}(\Omega) = e^{-i\alpha\hat{J}_z}e^{-i\beta\hat{J}_y}e^{-i\gamma\hat{J}_z}. \tag{2.24}$$

The integrals over Euler angles Ω are evaluated numerically.

2.3 Generator Coordinate Method

To obtain more precise wave functions and energies, we perform the generator coordinate method (GCM) [84] by employing the quadrupole deformation parameters β and γ as the generator coordinates. The wave function of GCM is expressed as

$$\Psi^{J^\Pi}_{Mn} = \sum_i \sum_K c^{J^\Pi}_{Kin} \Phi^{J^\Pi}_{MK}(\beta_i, \gamma_i), \tag{2.25}$$

where the unknown coefficients $c^{J^\Pi}_{Kin}$ and eigenenergies $E^{J^\Pi}_n$ are obtained by solving the Hill-Wheeler equation [85],

$$\begin{aligned} \sum_{i'K'} H^{J^\Pi}_{KiK'i'} c^J_{K'i'n} &= E^{J^\Pi}_n \sum_{i'K'} N^{J^\Pi}_{KiK'i'} c^{J^\Pi}_{K'i'n}, \\ H^{J^\Pi}_{KiK'i'} &= \langle \Phi^{J^\Pi}_{MK}(\beta_i, \gamma_i) | \hat{H} | \Phi^{J^\Pi}_{MK'}(\beta_{i'}, \gamma_{i'}) \rangle \,, \\ N^{J^\Pi}_{KiK'i'} &= \langle \Phi^{J^\Pi}_{MK}(\beta_i, \gamma_i) | \Phi^{J^\Pi}_{MK'}(\beta_{i'}, \gamma_{i'}) \rangle \,. \end{aligned} \tag{2.26}$$

We also calculate the overlap between $\Psi^{J^\Pi}_{Mn}$ and the basis wave function of the GCM $\Phi^{J^\Pi}_{MK}(\beta_i, \gamma_i)$,

$$| \langle \Phi^{J^\Pi}_{MK}(\beta, \gamma) | \Psi^{J^\Pi}_{Mn} \rangle |^2 / \langle \Phi^{J^\Pi}_{MK}(\beta, \gamma) | \Phi^{J^\Pi}_{MK}(\beta, \gamma) \rangle \,, \tag{2.27}$$

to discuss the dominant configuration in each state described by $\Psi^{J^\Pi}_{Mn}$.

When a rotational band is formed and its moment of inertia is large, the excited member state decays into lower-lying levels with large electric quadrupole (E2) transition probability,

$$B(El; J_I \to J_F) = \sum_{M_F} \sum_{\mu} \left| \left\langle \Psi_F(J_F, M_F) \middle| \sum_{i=1}^{A} r_i^l Y_{l\mu}(\mathbf{r}_i) \middle| \Psi_I(J_I, M_I) \right\rangle \right|^2 . \tag{2.28}$$

2.4 Single-Particle Properties

The neutron single-particle orbits of the intrinsic wave functions $\Phi_{int}(\beta, \gamma)$ provide us the motion of the valence neutrons around the core nucleus. In order to construct a single-particle Hamiltonian, we first transform the single-particle wave packet φ_i to the orthonormalized basis,

$$\widetilde{\varphi}_\alpha = \frac{1}{\sqrt{\lambda_\alpha}} \sum_{i=1}^{A} g_{i\alpha} \varphi_i. \tag{2.29}$$

Here, λ_α and $g_{i\alpha}$ are the eigenvalues and eigenvectors of the overlap matrix $B_{ij} = \langle \varphi_i | \varphi_j \rangle$. Using this basis, the Hartree-Fock single-particle Hamiltonian is derived,

$$\begin{aligned} h_{\alpha\beta} &= \langle \widetilde{\varphi}_\alpha | \hat{t} | \widetilde{\varphi}_\beta \rangle + \sum_{\gamma=1}^{A} \langle \widetilde{\varphi}_\alpha \widetilde{\varphi}_\gamma | \hat{v}^N + \hat{v}^C | \widetilde{\varphi}_\beta \widetilde{\varphi}_\gamma - \widetilde{\varphi}_\gamma \widetilde{\varphi}_\beta \rangle \\ &\quad + \frac{1}{2} \sum_{\gamma,\delta=1}^{A} \langle \widetilde{\varphi}_\gamma \widetilde{\varphi}_\delta | \widetilde{\varphi}^*_\alpha \widetilde{\varphi}_\beta \frac{\delta \hat{v}^N}{\delta \rho} | \widetilde{\varphi}_\gamma \widetilde{\varphi}_\delta - \widetilde{\varphi}_\delta \widetilde{\varphi}_\gamma \rangle. \end{aligned} \tag{2.30}$$

The eigenvalues ϵ_s and eigenvectors $f_{\alpha s}$ of $h_{\alpha\beta}$ give the single-particle energies and the single-particle orbits, $\widetilde{\phi}_s = \sum_{\alpha=1}^{A} f_{\alpha s} \widetilde{\varphi}_\alpha$. We calculate the amount of the positive-parity component in the single-particle orbit,

$$p^+ = |\langle \widetilde{\phi}_s | \frac{1 + P_x}{2} | \widetilde{\phi}_s \rangle|^2, \tag{2.31}$$

and angular momenta in the intrinsic frame,

$$j(j+1) = \langle\widetilde{\phi}_s|\hat{j}^2|\widetilde{\phi}_s\rangle, \quad |j_z| = \sqrt{\langle\widetilde{\phi}_s|\hat{j}_z^2|\widetilde{\phi}_s\rangle}, \tag{2.32}$$

$$l(l+1) = \langle\widetilde{\phi}_s|\hat{l}^2|\widetilde{\phi}_s\rangle, \quad |l_z| = \sqrt{\langle\widetilde{\phi}_s|\hat{l}_z^2|\widetilde{\phi}_s\rangle}, \tag{2.33}$$

which are used to discuss the properties of the single-particle orbits.

2.5 Reduced Width Amplitude

Using the GCM wave function, we calculate the reduced width amplitudes (RWA) $y_{lj^\pi_n}(r)$ for the ^{4}He + ^{10,12}Be and ^{6}He + ^{8,10}Be decays which are defined as,

$$y_{lj^\pi_n}(r) = \sqrt{\frac{A!}{A_{\rm He}!A_{\rm Be}!}}\langle\phi_{\rm He}[\phi_{\rm Be}(j^\pi_n)Y_{l0}(\hat{r})]_{J^\Pi M}|\Psi^{J\Pi}_{Mn}\rangle, \tag{2.34}$$

where $\phi_{\rm He}$ denotes the ground state wave function for ^{4}He or ^{6}He, and $\phi_{\rm Be}(j^\pi_n)$ denotes the wave functions for daughter nucleus Be isotopes with spin-parity j^π_n. $Y_{l0}(\hat{r})$ is the orbital angular momentum of the inter-cluster motion, and it is coupled with the angular momentum of Be(j^π_n) to yield the total spin-parity J^Π. $A_{\rm He}$ and $A_{\rm Be}$ are the mass numbers of He and Be, respectively. The spectroscopic factor S is defined by the integral of the RWA,

$$S = \int_0^\infty r^2|y_{lj^\pi_n}(r)|^2dr. \tag{2.35}$$

The reduced width $\gamma_{lj^\pi_n}$ is given by the square of the RWA,

$$\gamma^2_{lj^\pi_n}(a) = \frac{\hbar^2}{2\mu a}|ay_{lj^\pi_n}(a)|^2, \tag{2.36}$$

where μ and a denotes the reduced mass and the channel radius, respectively. The partial decay width is a product of the reduced width and the penetration factor $P_l(a)$,

$$\Gamma_{lj^\pi_n} = 2P_l(a)\gamma^2_{lj^\pi_n}(a), \quad P_l(a) = \frac{ka}{F_l^2(ka)+G_l^2(ka)}, \tag{2.37}$$

where P_l is given by the Coulomb regular and irregular wave functions F_l and G_l. The wave number k is determined by the decay Q-value and the reduced mass μ as $k = \sqrt{2\mu E_Q}$.

In the case of ^{14}C, to reduce the computational cost we calculate the RWA employing an approximate method given in Ref. [86]. In this method the antisymmetrization effect is neglected by choosing sufficiently large inter-cluster distance a, and the RWA is approximated by the overlap between the GCM wave function and the Brink-Bloch wave function $\Phi^{J\pi jl}_{BB}(a)$ in which He and Be clusters are placed with the inter-cluster distance a,

$$|ay_{lj^{\pi'}}(a)|^2 \simeq \sqrt{\frac{\gamma}{2\pi}}|\,\langle\Phi^{J\pi jl}_{BB}(a)|\Psi^{J\pi}_{Mn}\rangle\,|^2, \tag{2.38}$$

$$\gamma = \frac{A_{\rm He}A_{\rm Be}}{A}\nu_{BB}.$$

where ν_{BB} denotes the width parameter of the Gaussian wave packet of Brink-Bloch wave function.

The Brink-Bloch wave function is constructed as follows. First, the intrinsic wave function for ^{10}Be and ^{8}Be denoted by $\psi_{\rm Be}$ are generated by the AMD energy variation. The intrinsic wave function of Be is approximated by a single AMD Slater determinant with spherical Gaussian wave packets with the width parameter $\nu_{BB} = 0.16$ fm^{-2}. In the case of ^{8}Be, the wave functions of the 0^+_1 and 2^+_1 states are calculated by the bound-state approximation. The density distribution of obtained intrinsic wave function of ^{8}Be is shown in Fig. 2.1(a) in which the distance between two α clusters is approximately 3.4 fm. For the positive parity states of ^{10}Be, we obtained two different intrinsic wave functions shown in Fig. 2.1 (b) and (c) in which two valence neutrons occupy so-called π- and σ-orbits, respectively. We regard that the former correspond to the ground band (the 0^+_1, 2^+_1, and 4^+_1 states), while the latter is the excited band (the 0^+_2, 2^+_3, and 4^+_2 states). For the negative parity states of ^{10}Be, we obtain an intrinsic wave function shown in Fig. 2.1 (d) and (e) in which one of two valence neutrons occupies π-orbit and the other occupies σ-orbit. Next, they are projected to the eigenstate of the angular momentum j^π as $\phi_{\rm Be}(j^\pi_n) = \hat{P}^{j\pi}_{mk}\psi_{\rm Be}$, where we approximate that the Be wave functions are the eigenstates of the angular momentum $\hat{j}_z$ in the intrinsic frame. The eigenvalue k is assumed to be $k = 0$ in the positive-parity states and $k = -1$ in the negative-parity states. The construction of the wave function of ^{4}He and ^{6}He is explained later. The Brink-Bloch wave function is constructed by placing these He and Be wave functions with the inter-cluster distance a,

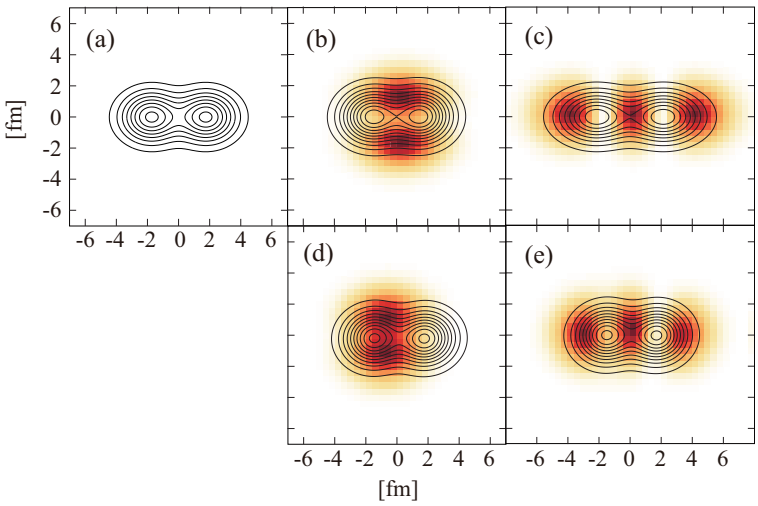

Figure 2.1: Density distribution of (a) ^{8}Be, the positive parity states of ^{10}Be with valence neutrons in (b) π-orbit and (c) σ-orbit, and (d)(e) negative parity states of ^{10}Be. The contour lines show the proton density distributions. The color plots of (b)(c) show the single-particle orbits occupied by the most weakly bound neutron. In negative parity state, the color plots of (d) show the single-particle orbits occupied by the most weakly bound neutron, and those of (e) show the other valence neutron.

$$\Phi^{jm}_{BB}(a) = \mathcal{A}\left\{\phi_{\rm He}\left(-\frac{A_{\rm Be}}{A}a\right)\hat{P}^{j}_{mk}\psi_{\rm Be}\left(\frac{A_{\rm He}}{A}a\right)\right\}, \tag{2.39}$$

and projected to the eigenstate of the total spin-parity J^Π as $\hat{P}^{J^\Pi}_{Mm}\Phi^{jm}_{BB}(a)$. We construct the wave function, in which the angular momentum l of the inter-cluster motion and the angular momentum j of Be are coupled to the total spin-parity J^Π, by summing up for all possible values of m,

$$\Phi^{J\pi jl}_{BB}(a) = n\frac{2l+1}{2J+1}\sum_m C^{Jm}_{l0jm}\hat{P}^{J^\pi}_{Mm}\Phi^{jm}_{BB}(a), \tag{2.40}$$

where C^{Jm}_{l0jm} and n denotes the Clebsch-Gordan coefficient and the normalization factor.

Generally, the partial decay width should be independent on the choice of the channel radius. However, in the practical calculation, the channel radius must be properly chosen to stabilize the results because of the following two problems. Firstly, the channel radius should not be too large value, because we adopt the bound-state approximation in the GCM calculation and hence the wave function is not correct at large inter-cluster distance. Secondly, the channel radius a should not

be too small, because the antisymmetrization effect cannot be neglected and the approximation is not valid. Therefore, we adopted two different values for the channel radius. The first choice is $a = 5.2$ fm which is common to the value used in the R-matrix analysis of the π-bond linear chain candidates observed in Ref. [69] and close to that in Ref. [71]. Unfortunately, this choice of channel radius is found inappropriate for the analysis of the σ-bond linear chain. Because σ-bond linear chain is dominated by the $^{10}\mathrm{Be}(0_2^+, 2_3^+) + \alpha$ channels and $^{10}\mathrm{Be}(0_2^+, 2_3^+)$ have larger radii than the ground state, the larger channel radius should be used to avoid the antisymmerzation effect. Hence, we used $a = 6.0$ fm for the analysis of σ-bond linear chain.

Next, we explain how the wave functions of ^{4}He and ^{6}He clusters are constructed when the RWA in ^{14}C is calculated by the approximation. The wave function of ^{4}He is approximated by a $(0s_{1/2})^4$ wave function of harmonic oscillator which is represented by the Gaussian wave packet with the width of $\nu_{BB} = 0.16$ fm^{-2},

$$\phi_{0s}(\mathbf{r}) = (2\nu/\pi)^{3/4} e^{-\nu r^2} \otimes \chi. \tag{2.41}$$

The ground state of ^{6}He is approximated by a $(0s_{1/2})^4(0p_{3/2})^2$ configuration as

$$\phi_{\mathrm{He}}^{J=0} = \mathcal{A}\{(0s_{1/2})^4[0p_{3/2} \otimes 0p_{3/2}]^{J=0}\} \tag{2.42}$$

where $0p_{3/2}$ is also the eigen function of harmonic oscillator. In the practical calculation, we do not use harmonic oscillator wave functions directly, but the $0p_{3/2}$ wave function is represented by the sum of the infinitesimally shifted Gaussian wave packets $\phi_{0s}(\mathbf{r};\epsilon) = (2\nu/\pi)^{3/4}\exp -\nu(\mathbf{r} - \epsilon^2) \otimes \chi$. This greatly reduces the computational cost because it is possible to use ordinary computational code for AMD to calculate Eq. (2.38). The relationship between the shifted Gaussian wave packets and harmonic oscillator wave function is given as follows to the first order of the shift ϵ,

$$\begin{aligned}
\phi_{0s}(\mathbf{r};\epsilon) - \phi_{0s}(\mathbf{r};\mathbf{0}) &= \Big(\frac{2\nu}{\pi}\Big)^{3/4}\Big\{e^{-\nu(\mathbf{r}-\epsilon)^2} - e^{-\nu r^2}\Big\}\otimes(a\chi_\uparrow + b\chi_\downarrow) && (2.43)\\
&\simeq \Big(\frac{2\nu}{\pi}\Big)^{3/4} 2\nu\mathbf{r}\cdot\epsilon e^{-\nu r^2}\otimes(a\chi_\uparrow + b\chi_\downarrow) && (2.44)\\
&= -\Big(\frac{2\nu}{\pi}\Big)^{3/4} 2\nu r e^{-\nu r^2}\Big[a\mathcal{Y}_{1-1}(\epsilon)\phi_{p_{3/2}\ 3/2} + b\mathcal{Y}_{11}(\epsilon)\phi_{p_{3/2}\ -3/2}\\
&\quad +\sqrt{\frac{1}{3}}\Big\{b\mathcal{Y}_{1-1}(\epsilon) - \sqrt{2}a\mathcal{Y}_{10}(\epsilon)\Big\}\phi_{p_{3/2}\ 1/2}\\
&\quad +\sqrt{\frac{1}{3}}\Big\{a\mathcal{Y}_{11}(\epsilon) - \sqrt{2}b\mathcal{Y}_{10}(\epsilon)\Big\}\phi_{p_{3/2}\ -1/2}\\
&\quad +\sqrt{\frac{1}{3}}\Big\{\sqrt{2}b\mathcal{Y}_{1-1}(\epsilon) + a\mathcal{Y}_{10}(\epsilon)\Big\}\phi_{p_{1/2}\ 1/2}\\
&\quad -\sqrt{\frac{1}{3}}\Big\{\sqrt{2}a\mathcal{Y}_{11}(\epsilon) + b\mathcal{Y}_{10}(\epsilon)\Big\}\phi_{p_{1/2}\ -1/2}\Big] && (2.45)
\end{aligned}$$

where $\mathcal{Y}_{1m}(\mathbf{r})$ is the regular solid spherical harmonics,

$$\mathcal{Y}_{1m}(\mathbf{r}) = \sqrt{\frac{4\pi}{3}} r Y_{1m}(\hat{r}), \tag{2.46}$$

where $\phi_{p_{3/2}\ m}$ and $\phi_{p_{1/2}\ m}$ denote the $0p_{3/2}$ and $0p_{1/2}$ wave functions with the magnetic quantum number m. From Eq.(2.45), we see that $0p_{3/2}$ wave functions can be described by the sum of the $\phi_{0s}(\mathbf{r};\epsilon)$ with proper choice of a, b, and ϵ. Thus, Eq.(2.42) is represented by the sum of the Slater determinant of the shifted Gaussian packets. In the practical calculation the magnitude of ϵ is chosen as $|\epsilon| = 0.02$.

In the case of ^{16}C, we calculate the RWA employing the Laplace expansion method given in Ref. [87]. This method is applicable to unequal-sized and deformed clusters without any approximation. The RWA is obtained by using the GCM wave function,

$$y_{lj^\pi_n}(a) = \frac{1}{\sqrt{n_K^{J\Pi}}} \sum_{1\le j_1<...<j_A\le A} P(i_1,...,i_{C_1})[\chi_l(a;i_1,...,i_A)[N^{j_1\pi_1}(i_1,...,i_{C_1})N^{j_2\pi_2}(i_{C_1+1},...,i_A)]_{j_{12}}]_{JK}, \tag{2.47}$$

with the definitions of the overlaps:

$$\chi_l(a;i_1,...,i_A) = \left\langle \frac{\delta(r-a)}{r^2}Y_{l0}(\hat{r})\middle|\chi(\mathbf{r};i_1,...,i_A)\right\rangle, \tag{2.48}$$

$$N^{j_1\pi_1}_{m_1}(i_1,...,i_{C_1}) = \langle\Phi^{j_1\pi_1}_{m_1He}|\Psi_{He}(i_1,...,i_{C_1})\rangle, \tag{2.49}$$

$$N^{j_2\pi_2}_{m_2}(i_{C_1+1},...,i_A) = \langle\Phi^{j_2\pi_2}_{m_2Be}|\Psi_{Be}(i_1,...,i_{C_1})\rangle, \tag{2.50}$$

where $P(i_1,...,i_{C_1})$ and $n_K^{J\Pi}$ denotes the phase factor and normalization factor, respectively. The intrinsic wave functions for ^{10,12}Be and ^{4,6}He are generated by the AMD energy variation. For ^{12}Be, we obtain an intrinsic wave function in which two of four valence neutrons occupy π-orbit and the others occupy σ-orbit which is regarded as the ^{12}Be(0^+_1) and ^{12}Be(2^+_1). We also obtain another configuration having four valence neutrons in π-orbit, which we regard as ^{12}Be(0^+_2) and ^{12}Be(2^+_2). However, the decay width to these states are negligibly small, and hence, they are not discussed here. In following calculation, we assume that the ^{4}He and ^{6}He clusters are always $j^\pi = 0^+$.

We also calculate the neutron spectroscopic factors in order to compare with the α-cluster spectroscopic factors. The neutron spectroscopic factor S_n is written as

$$S_n = \int_0^\infty r^2|\varphi(r)|^2dr, \tag{2.51}$$

where $\varphi(r)$ is the overlap amplitude which is the overlap between the wave functions of nuclei with mass A and $A+1$,

$$\varphi(r) = \sqrt{A+1}\,\langle\Psi^{J'\Pi'}_{M'n'}(^{15}\mathrm{C})|\Psi^{J\Pi}_{Mn}(^{16}\mathrm{C})\rangle\,. \tag{2.52}$$

The intrinsic wave function for ^{15}C is generated by the AMD energy variation. The spin-parity of ^{15}C are chosen as $J'^{\Pi'} = 1/2^+$ (the ground state of ^{15}C) for positive-parity states of ^{16}C and $J'^{\Pi'} = 1/2^-, 3/2^-, 5/2^-$ for negative-parity states.

Chapter 3

Results

3.1 Results for ^{14}C

For ^{14}C, it is found that two types of linear-chain formation, π-bond and σ-bond linear chains, appear in positive-parity states. The calculated excitation energies, moment of inertia, and the α-decay widths of the linear-chain states are compared with the observed data for the first time. The properties of the π-bond linear-chain states reasonably agree with the observation, which convinces us of the linear-chain formation in ^{14}C. The negative-parity partners of the cluster states are also obtained by the energy variation. However, because of the mixing with the non-cluster configurations, these cluster configurations do not correspond to a single eigenstate in excited states. Thus, the present result does not show the linear-chain formation in the negative parity and further studies are in need to identify the structure of the observed negative-parity resonances. Also, we suggest the characteristic decay patterns and the Coulomb shift as the way to distinguish the π-bond and σ-bond linear chains. As a result, the σ-bond linear-chain is a good candidate for the higher-lying resonant states reported by a cluster-transfer experiment.

3.1.1 Energy surface and density distribution

Figure 3.1 (a) shows the energy surface as functions of quadrupole deformation parameters β and γ for $J^\pi = 0^+$ states obtained by the constraint variational calculation and angular momentum projection. The circles on the energy surfaces show the position of the energy minima.

The energy minimum of the 0^+ state is located at $(\beta, \gamma) = (0.36, 14^\circ)$ with the binding energy of 106.1 MeV. This intrinsic wave function is the most dominant component of the ground band as discussed in the next subsection. It is interesting that this minimum state is deformed, as seen in its intrinsic density distribution shown in Fig. 3.2 (a), despite of the neutron magic number $N = 8$. However, the deformation is not large enough to break the neutron magicity as the last valence neutron occupies p-wave that can be deduced from the density distribution of the valence neutron orbit shown in Fig. 3.2 (a).

In the oblate deformed region, the different structure which we call triangular configuration appears. Fig. 3.2 (b) shows the density distribution of the wave function located at $(\beta, \gamma) = (0.60, 25^\circ)$. The proton density distribution have triangular shape showing possible formation of 3α cluster core with triangle configuration. As shown in the next subsection, this intrinsic wave function becomes the most dominant component of the triangular band, which has large α reduced widths. Owing to the parity asymmetric shape, the valence proton orbit is an admixture of the positive- and negative-parity component as confirmed from the properties of the single-particle orbit listed in Table 3.1. The table also shows that two valence neutrons occupy positive-parity orbit (sd-shell) indicating the $2\hbar\omega$ excitation.

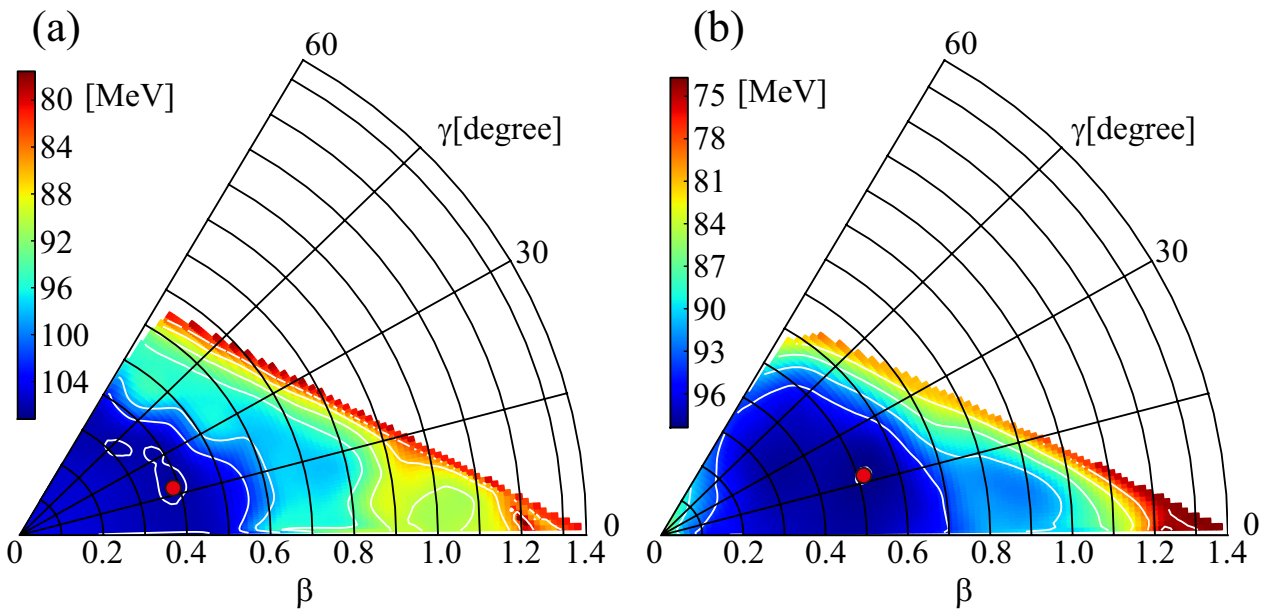

Figure 3.1: Angular momentum projected energy surface for (a) the $J^\pi = 0^+$ state and (b) $J^\pi = 1^-$ state as functions of quadrupole deformation parameters β and γ. The circles show the position of the energy minima.

In the strongly deformed region, the linear-chain configurations appear. There is an energy plateau around the local energy minimum at $(\beta, \gamma) = (1.00, 0^\circ)$ which approximately corresponds to the deformation ratio equal to 3 : 1. As clearly seen in its density distribution shown in Fig. 3.2 (c), this local energy minimum has pronounced 3α cluster structure with linear alignment. The properties of the proton single-particle orbit shows that the last two protons are excited into *sd*-shell, that is because of the Pauli principle in the linear-chain configuration. The density distribution and properties of the valence neutron orbits show that they correspond to the π-orbit of the molecular orbital picture which is schematically illustrated in Fig. 1.5. Namely, the valence neutron orbit is a linear combination of the *p*-wave perpendicular to the symmetry axis and has the angular momenta $|j_z| = 1.5$ and $|l_z| = 1.0$. It should be noted that the π-orbit of ^{14}C do not have parity symmetric distribution but is localized between the center and right α clusters. In other words, this configuration is the parity asymmetric and has $\alpha + ^{10}$Be-like structure, which is consistent with the discussion made in Refs. [55, 56]. Because this linear-chain configuration and the triangular configuration explained above have asymmetric internal structures, we expect that the corresponding negative-parity partners may exist and constitute the inversion doublets.

With further increase of the deformation, the other linear-chain configuration which we call σ-bond linear chain appears around $(\beta, \gamma) = (1.27, 0^\circ)$ which was not mentioned in Ref. [55]. This intrinsic wave function is the most dominant component of the σ-bond linear-chain band discussed in the next subsection. From the density distribution (Fig. 3.2 (d)), it is clear that this configuration has another valence neutron orbit that correspond to the σ-orbit which is a linear combination of *p*-wave parallel to the symmetry axis and has the angular momenta $|j_z| \approx 0.50$ and $|l_z| \approx 0$. It is interesting to note that this configuration has parity symmetric shape, and hence, do not have its negative-parity partner.

The energy minimum of the energy surface for the 1^- states (Fig. 3.1 (b)) is located at $(\beta, \gamma) = (0.52, 19^\circ)$ with the binding energy of -98.2 MeV, and its density distribution is described in Fig. 3.2(e). From Table 3.1, it can be seen that this minimum has the same proton configuration with the positive-parity minimum, but a neutron is excited into *sd*-shell from *p*-shell ($1p1h$ configuration).

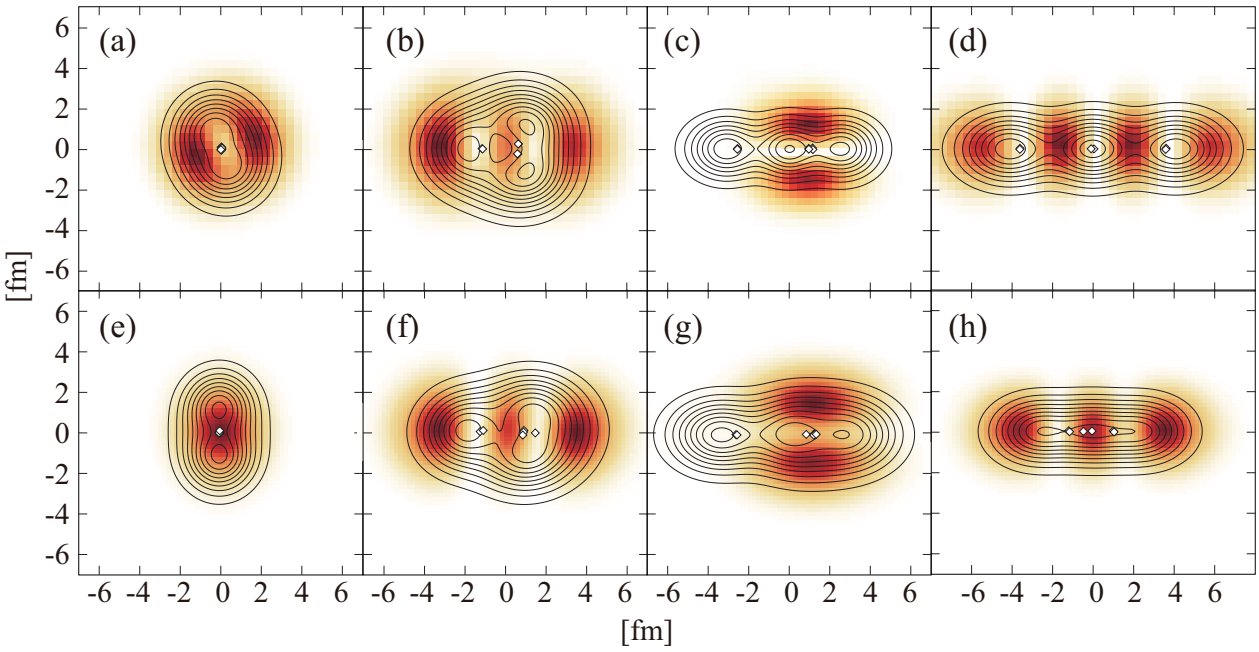

Figure 3.2: Density distribution of (a)-(d) positive-parity states and (e)-(h) negative-parity states. The contour lines show the proton density distributions. The color plots show the single-particle orbits occupied by the most weakly bound neutron. Open boxes show the centroids of the Gaussian wave packets describing protons.

In the deformed region, many different kinds of configurations appear. As reported in Ref. [55], it is found that these configurations are strongly mixed to each other and the unique band assignment of negative-parity states is impossible. Therefore, we do not discuss each configurations on the energy surface, but explain the negative-parity partner of the cluster configurations found in the positive parity. Because the triangular configuration and the π-bond linear-chain of the positive parity are parity asymmetric, their counterparts appear in the negative parity. Fig. 3.2 (f) and (g) show the triangular configuration and the π-bond linear-chain configuration in the negative-parity state located at $(\beta, \gamma) = (0.72, 14^\circ)$ and $(1.05, 3^\circ)$, respectively. Although the cluster cores are more distorted than the positive-parity states, their neutron single-particle configurations are similar to their positive-parity counterparts. However, as already mentioned and explained in the next subsection, these cluster configurations do not form single rotational band and are mixed with other configurations to yield several excited states. For example, the negative-parity π-bond linear-chain strongly mixes with the largely deformed non-cluster states such as the configuration shown in Fig. 3.2 (h).

Table 3.1: Properties of the most weakly bound proton and neutron orbits in the configurations shown in Fig. 3.2 (a)-(h). The column occ. shows the number of the nucleon occupying the orbit. When two valence nucleons occupy the almost degenerated orbits, the single-particle properties are averaged and occ. is equal to 2. Other columns show the single-particle energy ε in MeV, the amount of the positive-parity component p^+ and the angular momenta defined by Eqs. (2.31)-(2.33).

		occ.	ε	p^+	j	$\lvert j_z\rvert$	l	$\lvert l_z\rvert$
(a)	proton	2	−17.4	0.00	1.5	1.5	1.1	1.0
	neutron	2	−6.6	0.22	1.1	0.6	1.2	0.9
(b)	proton	2	−14.1	0.08	1.6	1.5	1.2	1.0
	neutron	2	−5.3	0.98	2.2	0.5	1.8	0.3
(c)	proton	2	−12.5	0.97	2.2	0.5	2.0	0.2
	neutron	2	−7.0	0.09	1.8	1.5	1.4	1.0
(d)	proton	2	−15.6	0.99	2.5	0.5	2.3	0.1
	neutron	2	−4.4	0.01	2.8	0.5	2.6	0.1
(e)	proton	2	−16.0	0.00	1.5	1.4	1.1	1.0
	neutron	1	−3.8	0.99	2.2	0.5	1.8	0.4
(f)	proton	1	−12.6	0.53	1.9	0.9	1.6	0.8
	neutron	2	−6.6	0.98	2.1	0.6	1.8	0.3
(g)	proton	1	−12.4	0.72	2.3	0.9	2.1	0.6
	neutron	2	−7.2	0.11	1.9	1.4	1.6	1.0
(h)	proton	1	−13.1	0.52	1.9	1.0	1.6	0.8
	neutron	2	−8.2	0.92	2.2	0.7	1.9	0.4

3.1.2 Energy spectrum

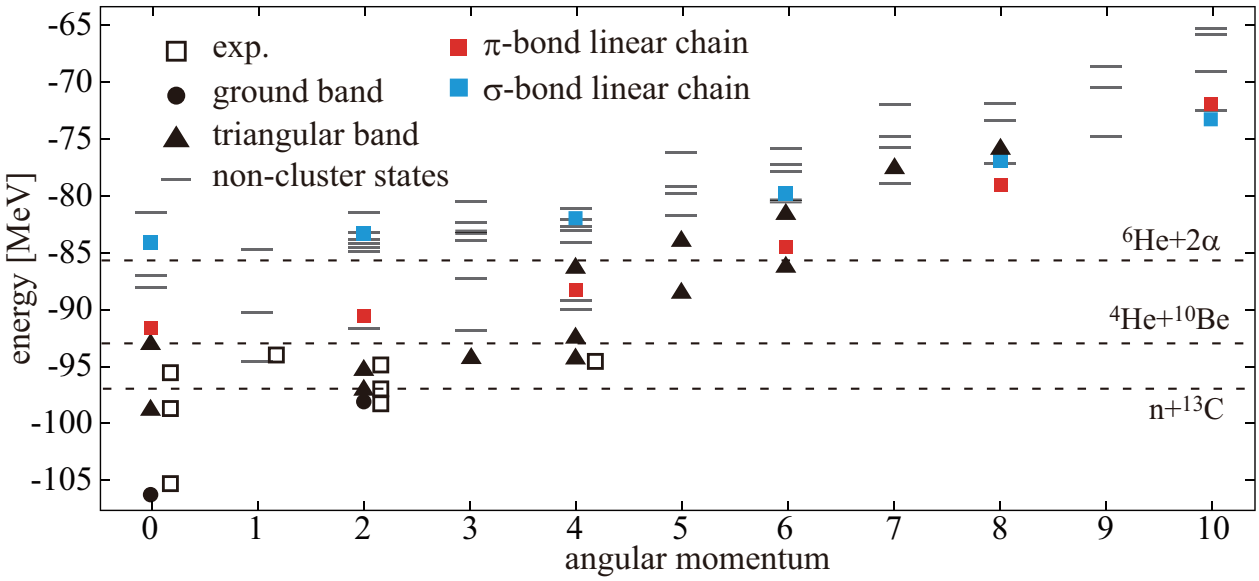

Figure 3.3: Positive-parity energy levels up to $J^\pi = 10^+$. Open boxes show the observed states with the definite spin-parity assignments taken from Ref. [88], and other symbols show the calculated result. The filled circles, triangles and filled boxes show the ground, triangular and linear-chain bands, while lines show the non-cluster states which have the reduced widths less than 0.08 MeV$^{1/2}$.

Figure 3.3 shows the spectrum of the positive-parity states obtained by the GCM calculation. The properties of the several selected states are listed in Table 3.2. The detail of the α reduced widths is given in next subsection. In the case of the positive-parity states, the cluster states are assigned in the rotational bands without uncertainty, because the band member states are connected by the strong $E2$ transitions as listed in Table 3.3.

The ground state and the first excited state (2_1^+) are dominantly composed of the configurations around the energy minimum of the energy surface. The ground state has the largest overlap (Eq. (2.27)) with the configuration shown in Fig. 3.2 (a) that amounts to 0.98, and the calculated binding energy is -106.3 MeV that is reasonably close to the observed value of -105.3 MeV. The excitation energy of the 2_1^+ state is also reasonably described. However, the calculated $B(E2)$ strength overestimates the observed value which may be due to the overestimation of the deformation. This overestimation of $B(E2)$ is common to ^{16}C.

Owing to its triaxial deformed shape, the triangular configuration generates the rotational bands built on the 0_2^+ and 2_3^+ states that are shown by triangles

Table 3.2: Excitation energies (MeV) and proton and neutron root-mean-square radii (fm) of several selected states. Numbers in the parenthesis are the observed data [88,89].

Band	J^π	E_x	r_p	r_n
Ground	0_1^+	0.00	2.53	2.58
	2_1^+	8.41	2.58	2.69
		(7.01)	(2.34)	
Triangular	0_2^+	7.49	2.67	2.92
$K^\pi = 0^+$	2_2^+	9.26	2.64	2.83
	4_1^+	12.00	2.65	2.89
Triangular	2_3^+	10.99	2.68	2.92
$K^\pi = 2^+$	3_1^+	12.03	2.68	2.92
	4_2^+	13.83	2.68	2.92
π-bond	0_4^+	14.64	3.27	3.20
linear chain	2_5^+	15.73	3.37	3.28
	4_5^+	17.98	3.33	3.24
	6_2^+	21.80	3.39	3.30
σ-bond	0_7^+	22.16	3.91	4.12
linear chain	2_{10}^+	22.93	4.02	4.21
	4_{11}^+	24.30	3.97	4.15

in Fig. 3.3. We call them $K^\pi = 0^+$ and 2^+ bands, respectively in the following, although the mixing of the K quantum number in their GCM wave functions is not negligible. Compared to the linear-chain states, these bands have less pronounced clustering and α clusters are considerably distorted, therefore the band head energies are well below the cluster thresholds. The member states have large overlap with the configuration shown in Fig. 3.2 (b) which amount to, for example, 0.91 in the case of the 0^+_2 state.

The linear-chain configurations generate two rotational bands in Fig. 3.3. The first one which we call π-bond linear-chain band is built on the 0^+_4 state at 14.6 MeV close to the α threshold energy and composed of the π-bond linear-chain configurations. The bandhead state (the 0^+_4 state) has large overlap with the configuration shown in Fig.3.2 (c) which amounts to 0.87. The other band which we call σ-bond linear-chain band is built on the 0^+_7 state at 22.2 MeV (about 9.18 MeV above the α threshold) and composed of the σ-bond linear-chain configurations shown in Fig.3.2 (d). This intrinsic wave function has the largest overlap with the band head state that amounts to 0.99. The $B(E2)$ strengths between the member states of these bands are rather strong compared to other in-band and inter-band transitions as listed in Table 3.3, which is consistent with the dominance of the strongly deformed intrinsic shapes with linear-chain configuration. Because the σ-bond linear chain is more strongly deformed than the π-bond linear chain, its in-band transition strengths are stronger than those of π-bond linear chain. Deference of the deformation also reflected to the moment of inertia; $\hbar^2/2\Im$ =179 and 98 keV for π-bond and σ-bond linear-chain bands, respectively. The π-bond linear-chain band is the candidate for the observed resonances and the comparison with the observation is discussed in Subsection 3.1.4.

Table 3.3: Calculated in-band $B(E2)$ strengths for the low-spin positive-parity states in unit of $e^2\text{fm}^4$. For the negative-parity states, the transitions between the low-spin cluster states (diamonds in Fig. 3.4) are shown and the transitions less than 10 $e^2\text{fm}^4$ are not shown. The number in parenthesis is the observed data [90].

	$J_i \to J_f$	$B(E2; J_i \to J_f)$
Ground $\to$ Ground	$2^+_1 \to 0^+_1$	8.1 (3.74)
Triangular $K^\pi = 0^+$	$2^+_2 \to 0^+_2$	7.6
$\to$ Triangular $K^\pi = 0^+$	$4^+_1 \to 2^+_2$	7.9
	$6^+_1 \to 4^+_2$	19.8
Triangular $K^\pi = 2^+$	$3^+_1 \to 2^+_3$	17.6
$\to$ Triangular $K^\pi = 2^+$	$4^+_2 \to 3^+_1$	8.5
	$4^+_2 \to 2^+_3$	5.4
π-bond linear chain	$2^+_5 \to 0^+_4$	165.5
$\to$ π-bond linear chain	$4^+_5 \to 2^+_5$	257.4
	$6^+_2 \to 4^+_5$	276.5
σ-bond linear chain	$2^+_{10} \to 0^+_7$	441.9
$\to$ σ-bond linear chain	$4^+_{11} \to 2^+_{10}$	655.9
Negative-parity states	$3^-_4 \to 1^-_3$	21.9
	$3^-_5 \to 1^-_3$	32.4
	$3^-_6 \to 1^-_5$	60.1
	$3^-_{10} \to 1^-_5$	31.5
	$5^-_2 \to 3^-_4$	63.0
	$5^-_4 \to 3^-_5$	54.5
	$5^-_7 \to 3^-_6$	53.9

In the case of the negative-parity states shown in Fig. 3.4, it is found that the α cluster configurations are mixed with other configurations and yield many excited states having non-negligible α reduced widths. As a result, the $E2$ transition strengths are also spread to several states, and it makes the band assignment ambiguous. For example, as listed in Table 3.3, there are two 3^- states that strongly decay to the 1^-_3 state. Therefore, applying the same standard with the positive parity, we classified the excited states which have larger α reduced widths than 0.10 $\text{MeV}^{1/2}$ as cluster states (diamond symbols). Those cluster states are shown by diamond symbols which are mainly composed of the configurations shown in Fig. 3.2(f), (g), (h) and other non-cluster config-

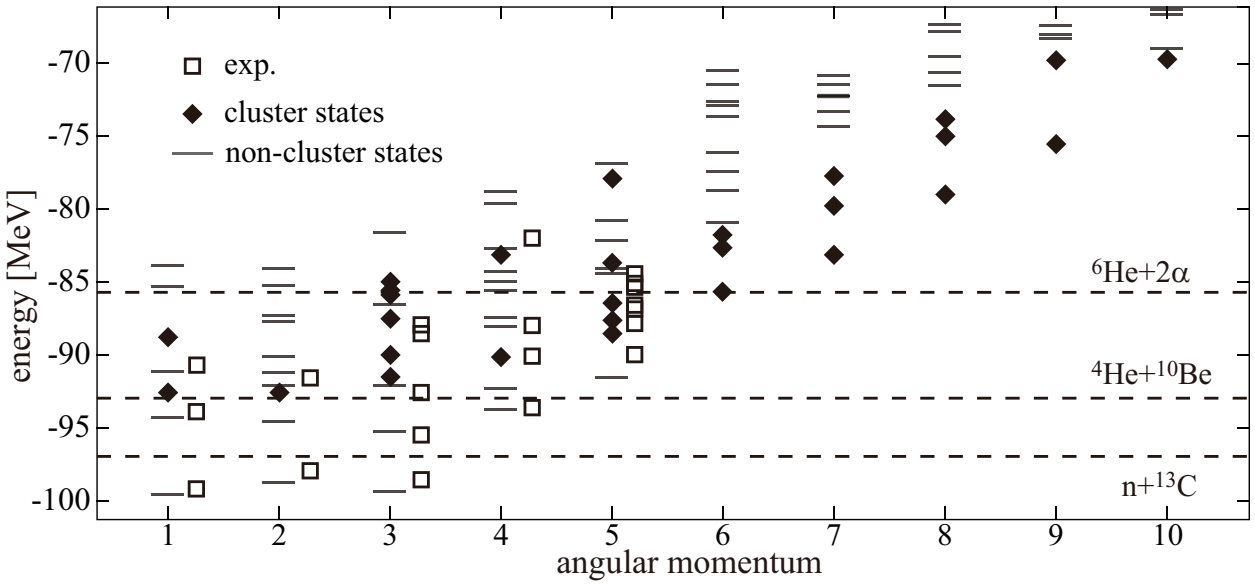

Figure 3.4: Negative-parity energy levels up to $J^\pi = 10^-$. Open boxes show the observed states with the definite spin-parity assignments taken from Refs. [53, 69–71, 88], and other symbols show the calculated result. The diamonds show the cluster states having non-negligible α reduced widths, while lines show the non-cluster states which have the reduced widths less than 0.10 $\mathrm{MeV}^{1/2}$.

urations. For example, the 1_3^- state has the largest overlap with the configuration shown in Fig. 3.2 (h) that amounts to 0.93. But, at the same time, this state also have large overlap with the triangular configuration shown in Fig. 3.2 (f) and the π-bond linear-chain shown in Fig. 3.2 (g) which amounts to 0.85 and 0.70, respectively. This means that these excited states are the mixture of cluster states and non-cluster states. As a result, the correspondence between the theory and experiment is not unique. We also performed an additional test calculation. We pickup the π-bond linear-chain configuration with positive parity shown in Fig. 3.2 (c) and artificially project it to the negative parity to estimate the energy of the ideal π-bond linear chain with negative parity. We see that the energy of the ideal linear-chain is too high to be assigned to the observed resonances. Thus, the present calculation does not support the formation of the linear chain in negative parity. The fragmentation of the cluster configurations can be more clearly seen in their α reduced widths which are discussed in the next subsection.

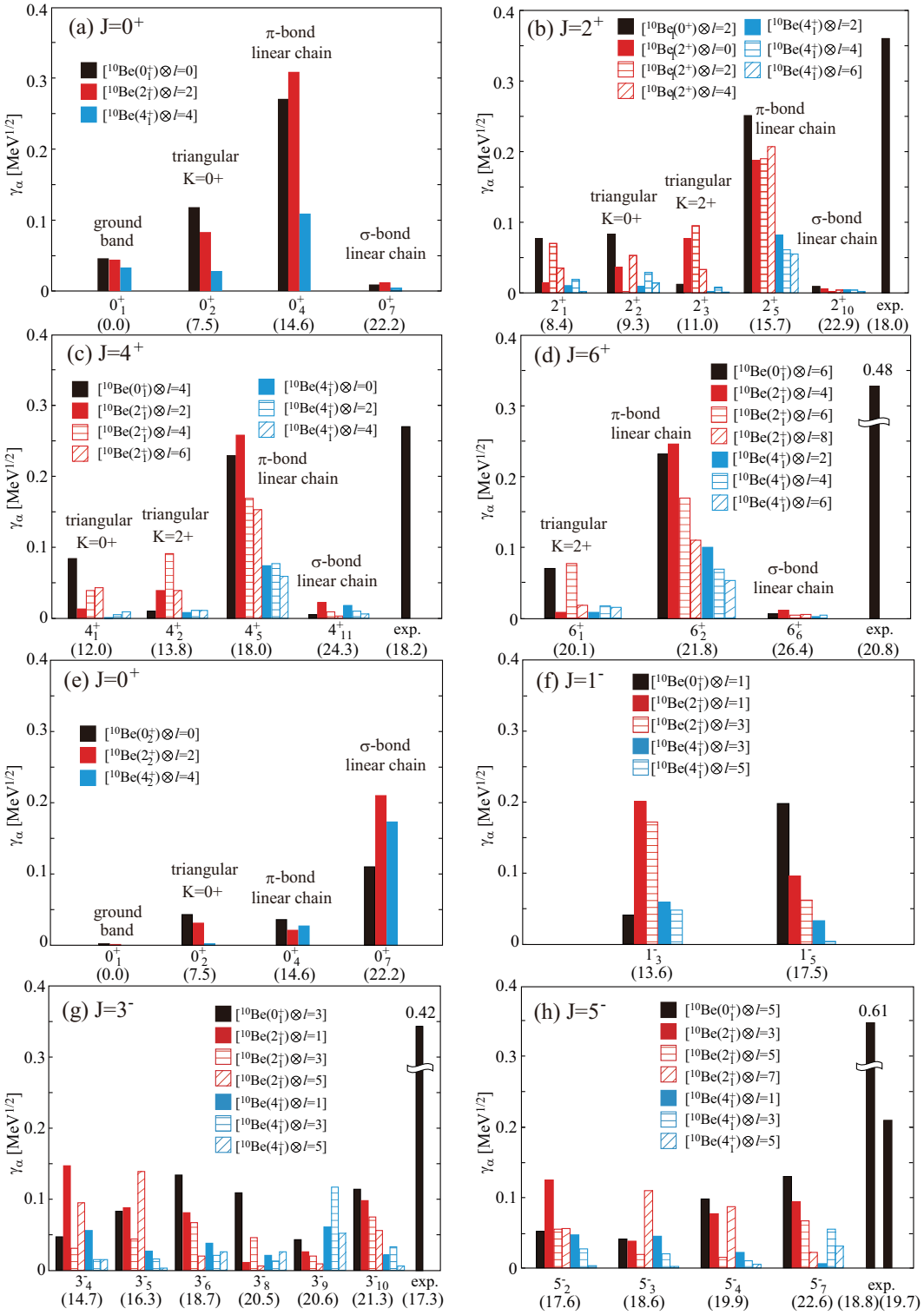

Figure 3.5: Calculated α-decay reduced widths compared with the observed widths reported in Ref. [69]. Panels (a)-(d) show the decay of the positive-parity states to the ground band of ^{10}Be (π-bonded ^{10}Be). Panel (e) shows the decay of the 0^+ states to the excited band of ^{10}Be (σ-bonded ^{10}Be). Panels (f)-(h) show the decay of the negative-parity states to the ground band of ^{10}Be (π-bonded ^{10}Be). Numbers in parenthesis show the excitation energy. The channel radius a is 5.2 fm.

3.1.3 Reduced width

Figure 3.5 shows the α reduced widths of several selected low-spin states with positive parity. The decay channels are indicated as $[^{10}\mathrm{Be}(j^\pi) \otimes l]$ where j^π and l denote the angular momenta of the ^{10}Be and the relative motion between ^{10}Be and α-particle, respectively. Here, except for the panel (e), ^{10}Be is assumed to have two neutrons in π-orbit, *i.e.* the ground band [39].

There are two prominent features to be noted in these results. The first is the magnitude of the reduced widths. The π-bond linear-chain band (the 0_4^+, 2_5^+, 4_5^+, and 6_2^+ states) have large reduced widths compared to the triangular bands and the ground state. It is also noted that the α reduced widths of other excited states are also smaller than the π-bond linear-chain band, and even smaller than or comparable with the triangular bands. Hence, in the calculated energy region, the π-bond linear chain band has the largest reduced width. In Fig. 3.5 (b)-(d), the observed reduced widths of the linear-chain candidates [69] are also shown for 2^+, 4^+, and 6^+ states. Since the decay to the ^{10}Be ground state was *assumed* in the R-matrix analysis made in Ref. [69], those values may be compared with the calculated results for the $[^{10}\mathrm{Be}(0_1^+) \otimes l]$ channel, and we see that only the π-bond linear-chain band can explain the magnitude of the observed reduced widths. The details are discussed in the next subsection.

It is also interesting to note that the other linear-chain band, *i.e.* the σ-bond linear-chain band, has suppressed reduced widths despite of their prominent α clustering. The reason is simple. Because the σ-bond linear-chain band does not have valence neutron in π-orbit, it is orthogonal to the decay channels to the ^{10}Be ground state that has π-orbit neutron. This is confirmed in Fig. 3.5 (e) where the reduced widths for the decays to the ^{10}Be with σ-bond (the excited rotational band, $^{10}\mathrm{Be}(0_2^+, 2_3^+, 4_2^+)$) are shown. Since other bands do not have valence neutrons in σ-orbit, their reduced widths are suppressed, and only the σ-bond linear-chain band has large widths. The details are discussed in Subsection 3.1.5.

Another point to be noted is the decay pattern of the π-bond linear-chain band. The reduced widths in the $[^{10}\mathrm{Be}(2_1^+) \otimes l]$ channels are as large as or even larger than those in the $[^{10}\mathrm{Be}(0_1^+) \otimes l]$ channel. This dominance of the $^{10}\mathrm{Be}(2_1^+)$ component in the π-bond linear-chain band is owe to its unique structure. When three α-particles are linearly aligned, because of the strong angular correlation between α-particles, the $^{10}\mathrm{Be}(2_1^+)$ and $^{10}\mathrm{Be}(4_1^+)$ components become large. This property is in contrast to the Hoyle state where α-particles are mutually orbiting with $l = 0$, and hence, the $^8\mathrm{Be}(0_1^+)$ component dominates [15]. Similar property of the linear-chain configuration were also discussed in ^{12}C [91]. Therefore, if the large contamination of the $^{10}\mathrm{Be}(2_1^+)$ component is confirmed, it will be a strong evidence for the linear-chain formation.

The $^{10}\mathrm{Be}(2_1^+)$ component in the triangular bands also show an interesting feature. There are two triangular bands with $K^\pi = 0^+$ and $K^\pi = 2^+$. The 0_2^+, 2_2^+ and 4_1^+ states are the member of the $K^\pi = 0^+$ band, while the 2_3^+, 4_2^+ and 6_1^+ are member of the $K^\pi = 2^+$ band. Here, it is clearly seen that the $^{10}\mathrm{Be}(0_1^+)$ component is dominant in the $K^\pi = 0^+$ band, while the $^{10}\mathrm{Be}(2_1^+)$ component is dominant in the $K^\pi = 2^+$ band. This feature is explained by Fig. 3.6. In the triangular bands, ^{4}He and ^{10}Be are placed in a triangular shape and the intrinsic z-axis is chosen to be perpendicular to the deformation axis of ^{10}Be. Since the K quantum number is the angular momentum directed to the intrinsic z-axis, K must be equal to the angular momentum of ^{10}Be. This makes the difference in the amount of the $^{10}\mathrm{Be}(2_1^+)$ component in the $K^\pi = 0^+$ and 2^+ bands.

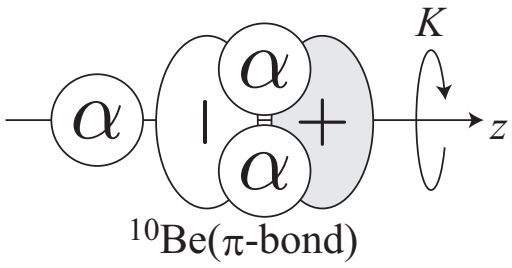

Figure 3.6: Schematic illustration which explains the relationship between the K quantum number and the angular momentum of ^{10}Be.

For the negative parity, we show the states which have the reduced widths larger than 0.10 $MeV^{1/2}$ in Fig. 3.5 (f)-(h). we can see that there are many states which have non-negligible α reduced widths, and not able to identify the linear-chain band. As already mentioned, the linear-chain configurations are mixed with the non-cluster configurations and yield many excited states as found in Ref. [55]. We also see that none of the calculated state can explain the observed reduced widths that are twice larger than the present results. This requires further theoretical study of the negative-parity states, although the current result looks negative to the linear-chain formation in the negative parity.

3.1.4 Comparison of the π-bond linear-chain states with the experiments

In this subsection, we discuss the assignment of the π-bond linear-chain band based on the latest experimental data. Freer *et al.* [69], Fritsch *et al.* [70] and more recently, Yamaguchi *et al.* [71] independently reported the resonances observed in the $\alpha + {}^{10}$Be scattering, which are shown by circles in Fig. 3.7 and summarized in Table 3.4. Freer *et al.* reported the 4^+ and 6^+ resonances at 18.22 and 20.80 MeV, respectively, while Fritsch *et al.* reported the 2^+ and 4^+ resonances at 15.0 and 19.0 MeV. A candidate for the 2^+ resonance at 17.95 MeV was also reported by Freer *et al.*, but not shown in Fig. 3.7 because the spin-parity assignment is not so firm. Yamaguchi *et al.* reported the 0^+, 2^+, and 4^+ resonances at 15.07, 16.22, and 18.87 MeV. The 4^+ energy is very close to that observed by Fritsch *et al.* and the 0^+ state may correspond to the Fritsch *et al.*'s 15.0 MeV state which was assigned as 2^+. We also note that the same resonances were also observed in the two-neutron transfer reaction [68] and cluster-transfer reactions [72,73], although the spin-parity assignment was not given.

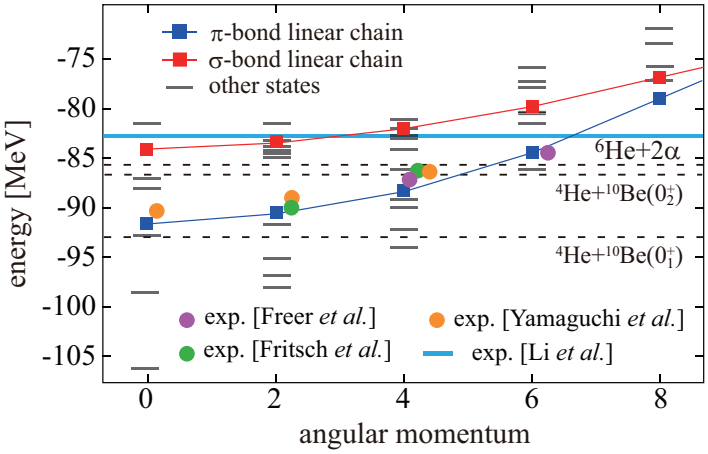

Figure 3.7: Positive-parity energy levels up to $J^\pi = 8^+$. Filled circles show the resonances with the definite spin-parity assignments observed in the α+^{10}Be resonant scattering [69–71]. Blue line shows the resonance at 22.5 MeV without spin-parity assignment observed by a cluster-transfer experiment [73]. Filled boxes show the calculated linear-chain bands, while lines show the other states. Only even angular momenta are shown.

We consider that they observed essentially the same resonances which are assigned to the π-bond linear-chain band from the following reasons. Firstly, it is clear that these resonance energies very nicely agree with those of the calculated π-bond linear-chain, regardless of the spin-parity assignments. Furthermore, the experiments show the large moments of inertia; $\hbar^2/2\Im = 116$ keV [69] and 190 keV [71]. The very large moment of inertia is consistent with the large deformation of the linear-chain band which reaches to 3:1 ratio of the deformation axes. In particular, the moment of inertia reported by Yamaguchi *et al.* ($\hbar^2/2\Im$ =190 keV) is very close to the present result ($\hbar^2/2\Im$ =179 keV). However, it is reminded that there is an experimental uncertainty in the assignment of the 15.0 MeV state ($J^\pi = 0^+$ or 2^+). Since the experimental spin-parity assignment of the broad resonances is no easy, it should be carefully discussed as it strongly affects the discussion of the moment of inertia.

Secondly, as listed in Table 3.4, the observed resonances have large α-decay widths to the

Table 3.4: Excitation energies (MeV) and α-decay widths (keV) up to $J^\pi = 8^+$ of the linear-chain states and the experiments. Γ_α shows the decay to the ground state (0^+_1) of ^{10}Be. Numbers in parentheses are tentative.

	π-bond linear chain			σ-bond linear chain		Exp. [69]		Exp. [70]		Exp. [71]	
J^π	E_x	Γ_α(5.2fm)	Γ_α(6.0fm)	E_x	Γ_α(6.0fm)	E_x	Γ_α	E_x	Γ_α	E_x	Γ_α
0^+	14.64	250	179	22.16	0.2					15.07	760
2^+	15.73	214	188	22.93	0.4	(17.95)	(760)	15.0	290	16.22	190
4^+	17.98	149	147	24.30	0.3	18.22	200	19.0	340	18.87	45
6^+	21.80	123	151	26.45	0.2	20.80	300				
8^+	27.25	77	120	29.39	0.2						

$\alpha + {}^{10}\mathrm{Be}(0^+_1)$ channel comparable with those of the calculated π-bond linear-chain. Unfortunately, experimental data are not quantitatively consistent to each other. In particular, the α-decay width reported by Yamaguhi *et al.* [71] are getting smaller with the increase of J much faster than the calculated ones while those reported in Refs. [69, 70] are getting larger. Nevertheless one would conclude that most of them are few hundreds keV which are the same order of magnitude with the calculated π-bond linear-chain. This is an evidence of the linear-chain formation, because theories predict no other states than the π-bond linear-chain states which have large α-decay widths in this energy region. It must be noted that the σ-bond linear-chain band has rather small decay widths to he $\alpha + {}^{10}\mathrm{Be}(0^+_1)$ channel, which distinguishes the σ-bond linear-chain from the π-bond linear-chain. The reason for this decay suppression will be explained in the next subsection.

Finally, theories predicted the decay of the π-bond linear-chain to the $\alpha + {}^{10}\mathrm{Be}(2^+_1)$ channel despite of the smaller decay Q-value (Table 3.5). This is because of the strong admixture of the $\alpha + {}^{10}\mathrm{Be}(0^+_1)$ and $\alpha + {}^{10}\mathrm{Be}(2^+_1)$ configurations in the π-bond linear-chain, which originates in the strong coupling nature of the linearly aligned alpha clusters. Experimentally, the width of the $\alpha + {}^{10}\mathrm{Be}(2^+_1)$ decay has not been measured, but Fritsch *et al.* reported the decay of the 4^+ resonance to the $\alpha + {}^{10}\mathrm{Be}(2^+_1)$ channel. Thus, the excitation energies, moment of inertia, and decay widths are consistent between the theory and the $\alpha + {}^{10}\mathrm{Be}$ scattering experiment, and hence, the formation of π-bond linear-chain in ^{14}C looks rather assured. However, it must be emphasized that further experimental studies are in need to resolve the inconsistency between the data and to firmly establish the linear-chain formation. In particular, the following points are essential and indispensable;

1. The assignment of the 15.0 MeV state, $J^\pi = 0^+$ or 2^+.

2. Quantitative agreement of the resonance widths between the experimental data and also with the theoretical results.

3. The confirmation of the decays to the inelastic channels and quantitative evaluation of the partial decay widths.

Table 3.5: Excitation energies (MeV) and α-decay widths (keV) to the 2^+_1 state of ^{10}Be.

	π-bond linear-chain			σ-bond linear-chain	
J^π	E_x	Γ_α(5.2fm)	Γ_α(6.0fm)	E_x	Γ_α(6.0fm)
0^+	14.64	-	-	22.16	0.6
2^+	15.73	-	-	22.93	0.2
4^+	17.98	118	111	24.30	1.8
6^+	21.80	256	271	26.45	0.4
8^+	27.25	397	421	29.39	0.8

3.1.5 Comparison of the σ-bond linear-chain states with the experiments

In addition to the candidates of the π-bond linear chain, several α-decaying resonances are reported above the α+^{10}Be(0^+_2) and ^{6}He + ^{8}Be(0^+_1) thresholds [63, 67, 72, 73]. In particular, quite recently, Li *et al.* [73] reported the decay property of a resonance located at 22.5 MeV, which provides new insight into the structure of the resonance. Since the spin-parity of the 22.5 MeV resonance has not been assigned, it is shown by blue line in Fig. 3.7. We see that its energy is close to the calculated 0^+, 2^+, 4^+, and 6^+ states of the σ-bond linear chain, although we cannot exclude the assignment to the 6^+ or 8^+ states of the π-bond linear chain.

In order to identify the structure of these resonances, we focus on the decay patterns of the π- and σ-bond linear chains. The reduced widths to various decay channels summarized in Figure 3.8 suggests unique decay patterns of the linear chains. From the panels (a) to (d), we see that all of the π-bond linear chain states decay to the ground band of ^{10}Be (0^+_1 and 2^+_1), but not to the excited band (0^+_2 and 2^+_3). On the other hand, the σ-bond linear chain has quite the opposite pattern; it decays to the excited band, but not to the ground band. This clearly distinguishes two linear-chains, and the reason of the difference is qualitatively understood from the intrinsic density distributions of the ^{10}Be and linear-chains shown in Figs. 2.1 and 3.2. Both of the ground band of ^{10}Be and π-bond linear chain has π-bonding neutrons, and hence, the π-bond linear chain can be described by the linear alignment of the ^{10}Be(0^+_1 and 2^+_1) and alpha cluster as illustrated in Fig.1.5. Since this configuration is orthogonal to the α+^{10}Be(0^+_1 and 2^+_1) the decay suppression to the α+^{10}Be(0^+_1 and 2^+_1) channels can be naturally understood. In the same way, the σ-bond linear chain can be described by the linear alignment of the ^{10}Be(0^+_2 and 2^+_3)+α which explains the decay pattern of the σ-bond linear chain.

Experimentally, it has been reported that several resonances above 20 MeV primary decay to the excited states of ^{10}Be around 6 MeV [63, 67, 72, 73] (see TABLE. I of Ref. [73] for the summary of the experimental data). In particular, Li *et al.* [73] reported the relative branching ratio of some resonances and showed that the 22.5 MeV resonance has approximately three times larger branching ratio to the 6 MeV state of ^{10}Be than those to the ^{10}Be(0^+_1) and ^{10}Be(2^+_1) shown in Fig. 1.7. Unfortunately, the experiment does not have enough energy resolution to identify the 6 MeV state of ^{10}Be out of the 0^+_2 (6.179 MeV), 2^+_2 (5.958 MeV), 1^-_1 (5.959 MeV), and 2^-_1 (6.263 MeV) states. However, if we assume that the 6 MeV state is the ^{10}Be(0^+_2), we consider that the decay pattern of the 22.5 MeV resonance is similar to the calculated σ-bond linear chain. To illustrate it, we calculated the decay of the linear chains to the ^{10}Be(0^+_1), ^{10}Be(2^+_1) and excited states around 6 MeV. The decay to the ^{10}Be(2^+_2) is not calculated because the triaxial deformation of ^{10}Be(2^+_2) [44] demands much computational cost. However, we expect that the decay to the ^{10}Be(2^+_2) should be negligible because its neutron configuration mismatches with the π- and σ-bond linear chains. In addition, we ensure that the decay widths into ^{10}Be(1^-_1) and ^{10}Be(2^-_1) are negligibly small.

Table 3.6 summarizes the calculated decay widths of the linear-chain states around 22.5 MeV. We see that the calculated σ-bond linear chain states have much larger decay width to the ^{10}Be(0_2^+) than to the ^{10}Be(0_1^+) and ^{10}Be(2_1^+) in order of magnitude. On the contrary, the π-bond linear chain states primary decay to the ^{10}Be(0_1^+) and ^{10}Be(2_1^+), which contradicts to the observation. Thus, the 22.5 MeV state is a good candidate for the σ-bond linear-chain. Of course, it must be emphasized that further experimental and theoretical studies are required to establish the σ-bond linear-chain. For example, the measurement of the absolute value of the partial decay widths is essential. Theoretically, the admixture of the π- and σ-bond configurations in ^{10}Be(0_1^+) and ^{10}Be(0_2^+) should be properly considered, as it quantitatively affects the decay branching ratio of the linear chains.

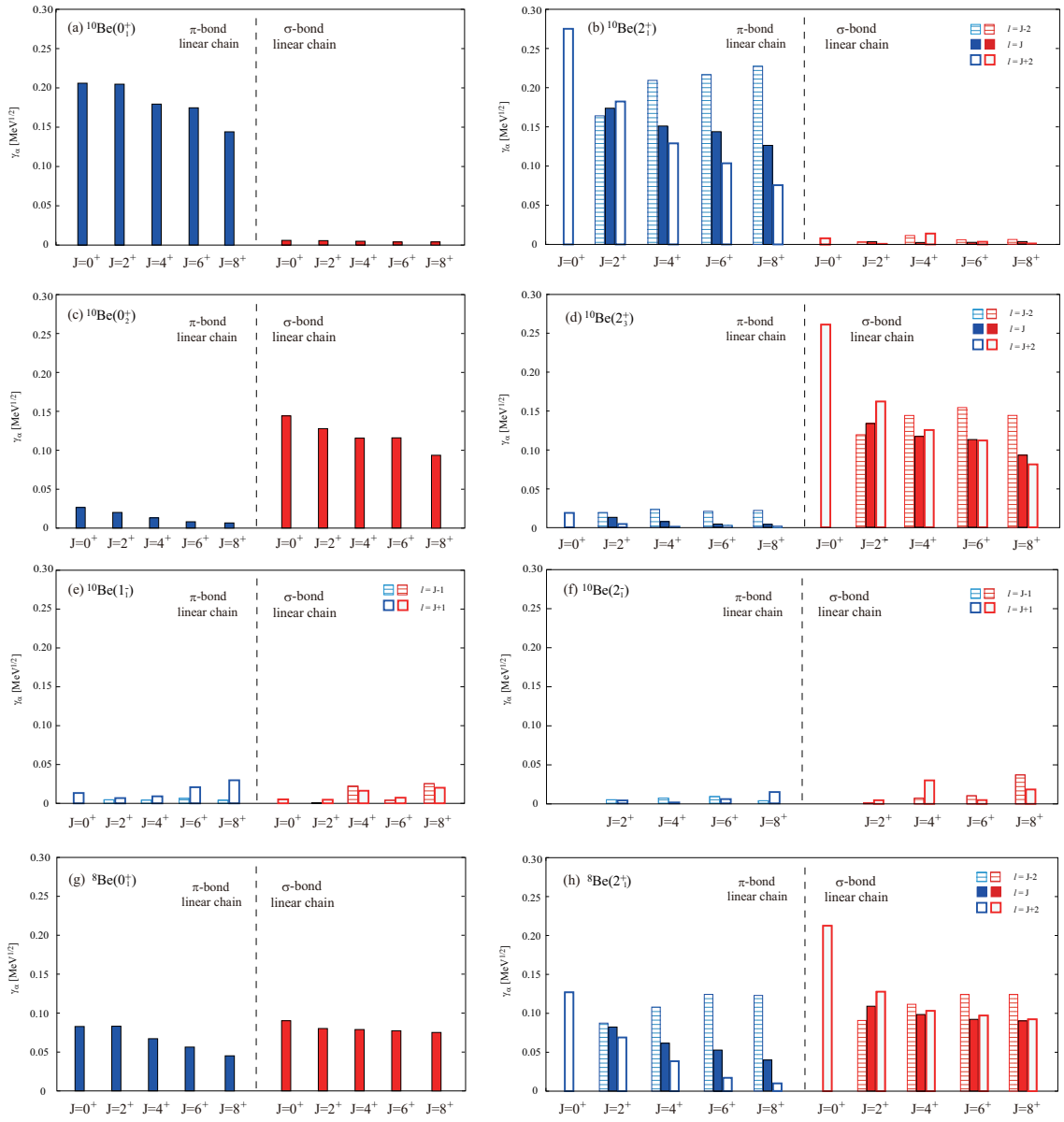

Figure 3.8: Calculated α- and ^{6}He-decay reduced widths up to $J^\pi = 8^+$. Panels (a)(b) show the decay to the ground band of ^{10}Be (π-bonded ^{10}Be). Panels (c)(d) show the decay to the excited band of ^{10}Be (σ-bonded ^{10}Be). Panels (e)(f) show the decay to the negative parity states of ^{10}Be. Panels (g)(h) show the decay to the ground band of ^{8}Be. The l denotes the relative motion between Be(2^+) and α-particle. The channel radius a is 6.0 fm.

Finally, we discuss the decays to ^{6}He + ^{8}Be and ^{5}He + ^{9}Be channels. Fig. 3.8 (g) and (h) show that both of the π- and σ-bond linear chains have large reduced widths in the ^{6}He + ^{8}Be channel, which is another interesting feature of the linear-chains. Therefore, the σ-bond linear chain and high-spin states ($J^\Pi \geq 6^+$) of π-bond linear chain which locate above the ^{6}He + ^{8}Be threshold should also decay to the three-body final state through the sequential two body decays, $^{14}C^* \to {}^6\mathrm{He} + {}^8\mathrm{Be} \to {}^6\mathrm{He} + \alpha + \alpha$. As listed in Table 3.6, the decay widths of the σ-bond linear chain to the ^{6}He + ^{8}Be channel are in the same order with those to the $\alpha + {}^{10}\mathrm{Be}(0^+_2)$ channel, and hence, the decay to ^{6}He + $\alpha + \alpha$ is another evidence of the linear-chain formation. We also comment on the decay to the ^{5}He + ^{9}Be channel (^{4}He + n + ^{9}Be) whose decay threshold locates very

close to that of the $^6\mathrm{He} + {}^8\mathrm{Be}$ channel. Theoretically, the decay width calculation for the odd-mass daughter nuclei demands much computational time, and hence, it is not performed in the present study. Nevertheless, we would expect that the decay of the σ-bond linear chain to the ^{9}Be ground state should be suppressed because of the π-bond nature of the ^{9}Be ground state. On the contrary, the decay to the first excited state of ^{9}Be should be relatively enhanced as it has the σ-bonding [41]. This decay pattern will also serve as another evidence of the σ-bond linear chain.

In conclusion, the π-bond linear-chain states decay to $^{10}\mathrm{Be}(\pi^2) + \alpha$ and higher-spin than the 6^+ states can decay to $^6\mathrm{He} + \alpha + \alpha$. In the case of the σ-bond linear-chain, they decay to $^{10}\mathrm{Be}(\sigma^2) + \alpha$ and $^6\mathrm{He} + \alpha + \alpha$ because all member states are above the both threshold energies. This decay pattern is an important evidence to show the formation of two linear-chains in ^{14}C.

Table 3.6: Partial decay widths (keV) in six different channels for (a) the σ-bond linear-chain states and (b) $J^\pi = 6^+, 8^+$ states of the π-bond linear-chain. The channel radius a is 6.0 fm.

(a) σ-bond linear-chain					
J^π	E_x	$\Gamma(^{10}\mathrm{Be}(0_1^+;\pi^2))$	$\Gamma(^{10}\mathrm{Be}(2_1^+;\pi^2))$	$\Gamma(^{10}\mathrm{Be}(0_2^+;\sigma^2))$	$\Gamma(^6\mathrm{He} + {}^8\mathrm{Be})$
0^+	22.16	0.2	0.6	136	38
2^+	22.93	0.4	0.2	99	29
4^+	24.30	0.3	1.8	63	23
6^+	26.45	0.2	0.4	42	17
8^+	29.39	0.2	0.8	17	13
(b) π-bond linear-chain					
6^+	21.80	151	271	0.0	0.0
8^+	27.25	120	421	0.0	1

3.1.6 Coulomb shift in ^{14}C-^{14}O

To establish the existence of the linear-chain structure, we also focus on the Coulomb shift in the mirror pair of ^{14}C and ^{14}O. Because of charge symmetry of nuclear interaction, the spectroscopic properties of mirror nuclei should be quite similar. However, the large difference in the excitation energies of the $s_{1/2}$ levels exists in the nucleus with the loosely bound proton and its mirror nucleus. It is due to the reduction of the Coulomb energy associated with the spatially extended s-wave, which is known as the Thomas-Ehrman shift [92–96]. The Thomas-Ehrman shift can be extended to the cluster structure based on the molecular orbital picture of Be isotopes because the σ-orbit is composed of the s-wave and d-wave. In fact, the Coulomb shifts of the ^{10}Be and ^{10}C was discussed from the viewpoint of the molecular orbital picture [97]. In this previous work, the Coulomb shift is prominent for the 0^+_1 state with the π-orbit nucleons which is dominated by the p-wave. On the other hand, the Coulomb shift of the 0^+_2 state with the σ-orbit is rather smaller than the 0^+_1 state. This reduction is due to the spatially extended σ-orbit which dominated by the s-wave and enhances the α-α clustering.

In this subsection we extend the discussion to the linear chain of ^{14}O. In particular, we expect large Thomas-Ehrman shift in the σ-bond linear chain because of its much larger spatially extent. However, the σ-orbit of ^{14}C-^{14}O does not have the s-wave but the pf-wave. Therefore, it is not clear that the σ-bond linear chain of ^{14}C-^{14}O shows the Thomas-Ehrman shift. Thus, we investigate Coulomb shifts of the linear-chain states in ^{14}C and ^{14}O based on the β-constraint AMD calculation. In particular, we focus on single-particle properties of the molecular orbits to clarify the origin of large energy shifts in the σ-bond linear chain.

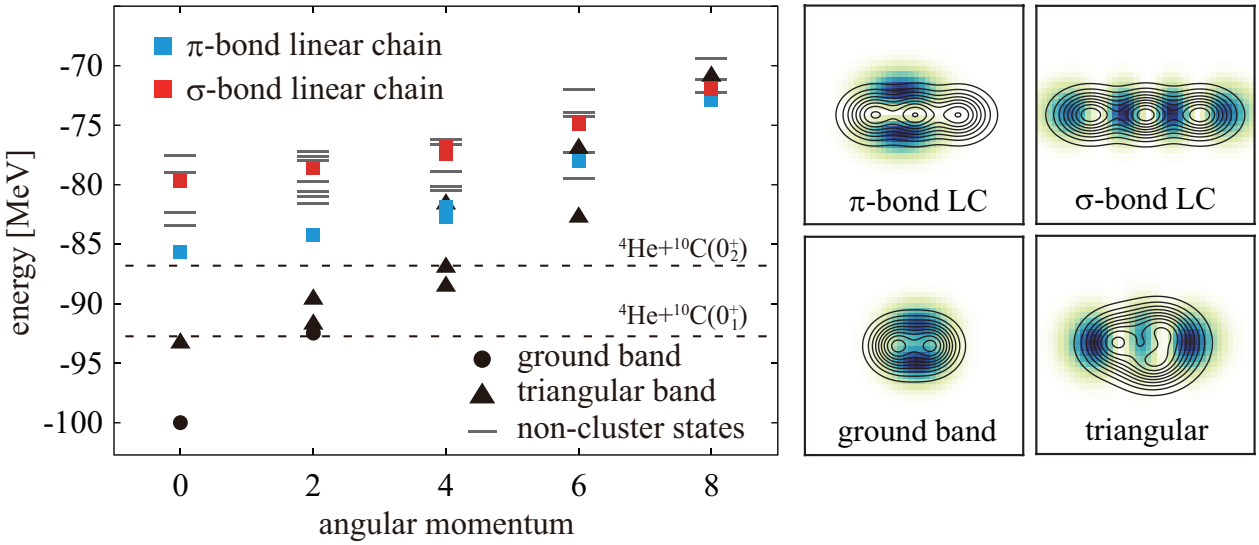

Figure 3.9: Left: Positive-parity energy levels of ^{14}O up to $J^\pi = 8^+$. The filled circles, triangles and boxes show the ground, triangular, and linear-chain bands, while lines show the non-cluster states. Dashed lines show theoretical threshold energies. Right: Density distributions of intrinsic wave functions in ^{14}O. Contour lines show the neutron density distribution and blue plots show the single-particle orbit occupied by the most weakly bound proton.

Figure 3.9 shows the calculated energy levels of ^{14}O as a function of the angular momentum (left panel). These energy levels are classified into three cluster bands and non-cluster states. The filled circles, triangles, blue and red boxes show the ground, triangular, π-bond, and σ-bond linear-chain band, respectively. Each band is dominantly composed of the intrinsic wave function shown in density distributions (right panels). It is found that these bands correspond to the triangular, π-

and σ-bond linear-chain bands in ^{14}C discussed in the previous subsection. To investigate the charge symmetry between ^{14}C and ^{14}O, we compare geometric properties of the linear-chain states with each other. For example, the root-mean-square radii of π- and σ-bond linear-chain states in ^{14}O(0^+) are 3.23 and 3.96 fm, which are almost same those in ^{14}C(0^+), 3.24 and 3.98 fm, respectively. In addition, the moments of inertia of the linear-chain bands in ^{14}O are $\hbar^2/2\Im = 177$ keV for π-bond linear-chain and 103 keV for σ-bond linear-chain, respectively. They are very close to those of ^{14}C, $\hbar^2/2\Im = 179$ and 98 keV. These suggest the good charge symmetry of the mirror pair of ^{14}C and ^{14}O. Binding energies and Coulomb energies of the ground states are listed in Table 3.7.

Table 3.7: Binding energies (MeV) and Coulomb energies (MeV) of the ground states in ^{14}C and ^{14}O.

	^{14}C	^{14}O	Difference
Binding energy	-106.19	-99.99	6.20
Coulomb energy	7.31	13.34	6.03

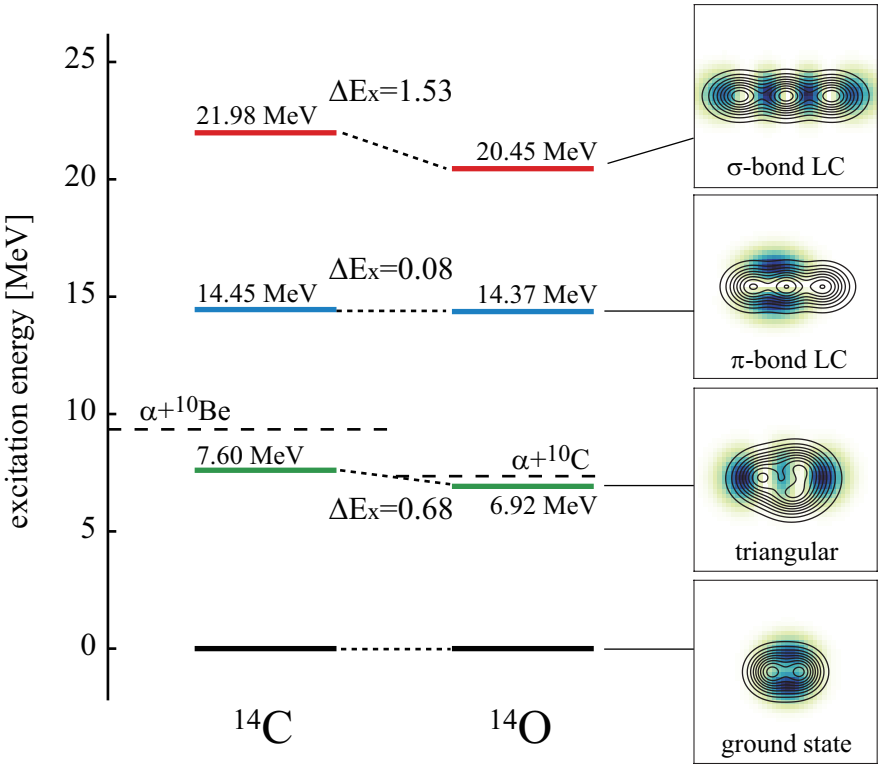

Figure 3.10: Energy spectra for $J^\pi = 0^+$ of ^{14}C (left levels) and ^{14}O (right levels). Levels are marked by an excitation energy in units of MeV. Dashed lines show theoretical thresholds.

Figure 3.10 shows the comparison of excitation energies between ^{14}C and ^{14}O for $J^\pi = 0^+$ states. The energy shift ΔE_x is defined as the difference of excitation energies,

$$\Delta E_x = \{E_n(^{14}\mathrm{C}^*) - E_{g.s.}(^{14}\mathrm{C})\} - \{E_n(^{14}\mathrm{O}^*) - E_{g.s.}(^{14}\mathrm{O})\}. \tag{3.1}$$

The energy shift of the σ-bond linear-chain, $\Delta E_x = 1.53$ MeV, is much larger than those of the triangular-cluster configuration ($\Delta E_x = 0.68$ MeV) and the π-bond linear-chain ($\Delta E_x = 0.08$

MeV). To discuss the origin of this large energy shift, we compare them with the Coulomb energy differences in Table 3.8. The eigenenergy can be divided into the Coulomb energy component and other components from Eq. (2.1),

$$E_n = \langle\Psi_n|\hat{H}|\Psi_n\rangle = \langle\hat{H}_n^{sym}\rangle + \langle\hat{v}_n^C\rangle\,, \tag{3.2}$$

$$\langle\hat{H}_n^{sym}\rangle = \langle\Psi_n|\hat{H}^{sym}|\Psi_n\rangle, \tag{3.3}$$

$$\langle\hat{v}_n^C\rangle = \langle\Psi_n|\hat{v}^C|\Psi_n\rangle. \tag{3.4}$$

If the mirror pair has the good charge symmetry,

$$\langle\hat{H}_n^{sym}\rangle\,(^{14}\mathrm{C}) \approx \langle\hat{H}_n^{sym}\rangle\,(^{14}\mathrm{O}), \tag{3.5}$$

the Eq. (3.1) can be rewritten as,

$$\Delta E_x \approx \{\langle\hat{v}_n^C\rangle\,(^{14}\mathrm{C}^*) - \langle\hat{v}_n^C\rangle\,(^{14}\mathrm{O}^*)\} - \{\langle\hat{v}_{g.s.}^C\rangle\,(^{14}\mathrm{C}) - \langle\hat{v}_{g.s.}^C\rangle\,(^{14}\mathrm{O})\} \equiv \Delta\,\langle\hat{v}_x^C\rangle\,. \tag{3.6}$$

The Coulomb energy difference of the σ-bond linear-chain, $\Delta\,\langle\hat{v}_x^C\rangle = 1.45$ MeV, is rather larger than those of other configurations. Note that this Coulomb energy difference is very close to the energy shift ($\Delta E_x = 1.53$ MeV). Therefore, we conclude that the large difference of the excitation energies in the σ-bond linear-chain dominantly comes from the Coulomb energy difference.

Table 3.8: Energy shifts ΔE_x (MeV) defined by Eq. (3.1) and Coulomb energy differences $\Delta\,\langle\hat{v}_x^C\rangle$ (MeV) defined by Eq. (3.6).

	0^+		2^+		4^+	
Band	ΔE_x	$\Delta\,\langle\hat{v}_x^C\rangle$	ΔE_x	$\Delta\,\langle\hat{v}_x^C\rangle$	ΔE_x	$\Delta\,\langle\hat{v}_x^C\rangle$
Ground	0	0	0.27	0.01		
Triangular (K=0)	0.68	0.72	0.85	0.73	1.04	0.83
Triangular (K=2)			0.85	0.76	1.09	0.77
π-bond	0.08	0.59	0.24	0.63	1.04	0.00
					0.27	0.30
σ-bond	1.53	1.45	1.31	1.04	1.49	0.34
					1.01	0.40

To get a deeper insight into the origin of the large Coulomb shift, we focus on single-particle properties listed in Table 3.9. We calculate the single-particle Coulomb energy,

$$\langle\hat{v}_{s.p.}^C\rangle = \langle\widetilde{\phi}_s|\hat{v}^C|\widetilde{\phi}_s\rangle, \tag{3.7}$$

and the root-mean-square radius of the single-particle orbit,

$$\sqrt{\langle r_{s.p.}^2\rangle} = \sqrt{\langle\widetilde{\phi}_s|\hat{r}^2|\widetilde{\phi}_s\rangle}. \tag{3.8}$$

We roughly estimate the Coulomb energy induced from two valence protons in the σ-orbit from Table 3.9,

$$-2\{\langle\hat{v}_{s.p.}^C\rangle\,(\sigma) - \langle\hat{v}_{s.p.}^C\rangle\,(g.s.)\} = -2\times(2.42 - 3.10) = 1.36, \tag{3.9}$$

which is also close to both the energy shift and the Coulomb energy difference, that is,

$$\Delta E_x \approx \Delta\,\langle\hat{v}_x^C\rangle \approx -2\{\langle\hat{v}_{s.p.}^C\rangle\,(\sigma) - \langle\hat{v}_{s.p.}^C\rangle\,(g.s.)\}. \tag{3.10}$$

This reduction of the Coulomb energy of the σ-orbit is derived from its large spatially extent. For example, the radius of the single particle of π-orbit, 2.95 fm, is smaller than those of ground state (3.11 fm) and triangular cluster configuration (3.90 fm). In contrast, the radius of the single-particle of the σ-orbit is 4.85 fm, which is huge. Therefore, the large energy difference of the σ-bond linear-chain can be illustrated by the reduction in the Coulomb energy associated with the spatially extended σ-orbit. Namely, we can see the Thomas-Ehrman shift in the σ-bond linear-chain states although the main component of the σ-orbit is pf-orbit in the case of ^{14}C-^{14}O. The Thomas-Ehrman shift is also suggested in the pair of ^{10}Be-^{10}C [97]. In the mirror pair of ^{10}Be and ^{10}C, the energy difference of the σ-bond states is $\Delta E_x = 1.0$ MeV against the ground state, which is a bit smaller than that of ^{14}C-^{14}O. The radius of the single-particle of the σ-orbit in ^{10}Be-^{10}C must be smaller than that in ^{14}C-^{14}O. Therefore, this difference may arise from the gap of the spatially extent of the σ-orbit between ^{10}Be-^{10}C and ^{14}C-^{14}O.

Table 3.9: Single-particle energies (MeV), radii (fm), and Coulomb energies (MeV) of the most weakly bound neutron (for ^{14}C) or proton (for ^{14}O).

	ϵ		$\sqrt{\langle r^2_{s.p.}\rangle}$		$\langle \hat{v}^C_{s.p.}\rangle$
	^{14}C	^{14}O	^{14}C	^{14}O	^{14}O
Ground state	-4.37	-1.82	3.12	3.11	3.10
Triangular	-5.32	-2.14	3.72	3.90	2.80
π-bond	-6.95	-3.92	2.92	2.95	2.96
σ-bond	-4.11	-1.76	4.85	4.85	2.42

In addition to 0^+ states, we show the comparison of excitation energies for $J^\pi = 2^+$ and 4^+ states in Figs. 3.11 and 3.12, respectively. For 2^+ state, the energy difference of the π-bond linear-chain states is also small ($\Delta E_x = 0.24$ MeV) and the same magnitude with that of the 2^+ member states in the ground band. In contrast, the larger difference of the σ-bond linear-chain states ($\Delta E_x = 1.31$ MeV) can be also seen clearly. It is close to the Coulomb energy difference, 1.04 MeV in Table 3.8. The same tendency as the 0^+ states appear in the 2^+ states, i.e., the energy shift is negligibly small for the π-bond linear-chain states, while it is prominent for the σ-bond linear-chain states because of the Coulomb energy reduction. For 4^+ state, π- and σ-bond linear-chain states of ^{14}O are fragmented into two states because of the coupling with other configuration. The lower σ-bond linear-chain state shows the large energy shift, 1.49 MeV. However, it cannot be explained as the Coulomb energy reduction because the Coulomb energy difference is 0.34 MeV, too small. It shows that the mirror system does not have the good charge symmetry written by Eq. (3.5) for 4^+ state.

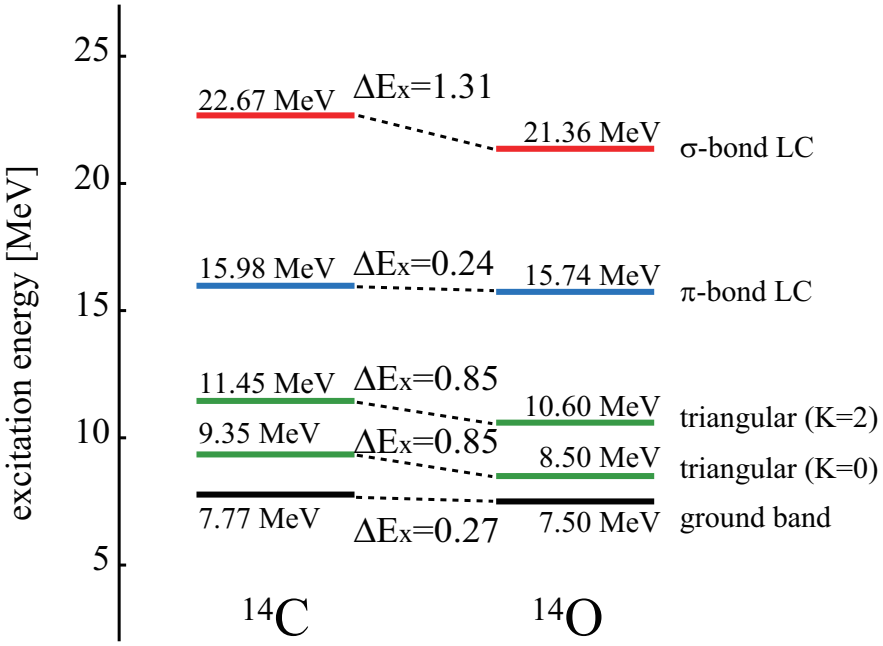

Figure 3.11: Energy spectra for $J^{\pi} = 2^{+}$ of ^{14}C and ^{14}O.

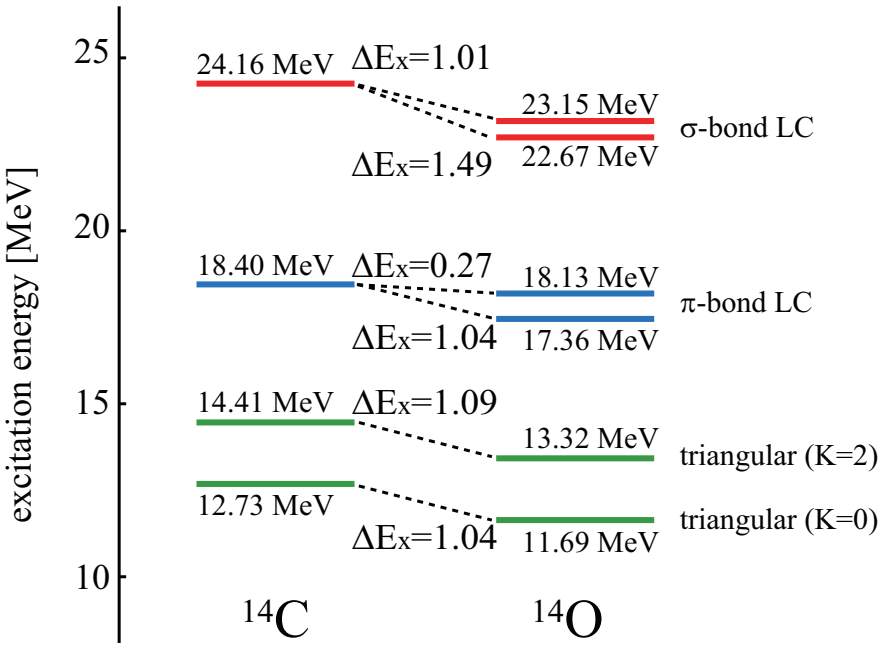

Figure 3.12: Energy spectra for $J^{\pi} = 4^{+}$ of ^{14}C and ^{14}O.

3.2 Results for ^{16}C

For ^{16}C, it is found that the positive-parity linear-chain states have the $(3/2^-_\pi)^2(1/2^-_\sigma)^2$ configuration and primary decay to ^{12}Be(2^+_1) as well as to ^{12}Be(g.s.) by α-particle emission. Moreover, we show that they also decay via the ^{6}He + ^{10}Be channel. In the negative-parity states, it is found that two types of the linear-chains exist. One has the valence neutrons occupying the molecular orbits $(3/2^-_\pi)^2(1/2^-_\sigma)(3/2^+_\pi)$, while the other's configuration cannot be explained in terms of the molecular orbits because of the strong parity mixing. Their α and ^{6}He reduced widths are sufficiently large to be distinguished from other non-cluster states although they are smaller than those of the positive-parity linear chain.

3.2.1 Energy surface and density distribution

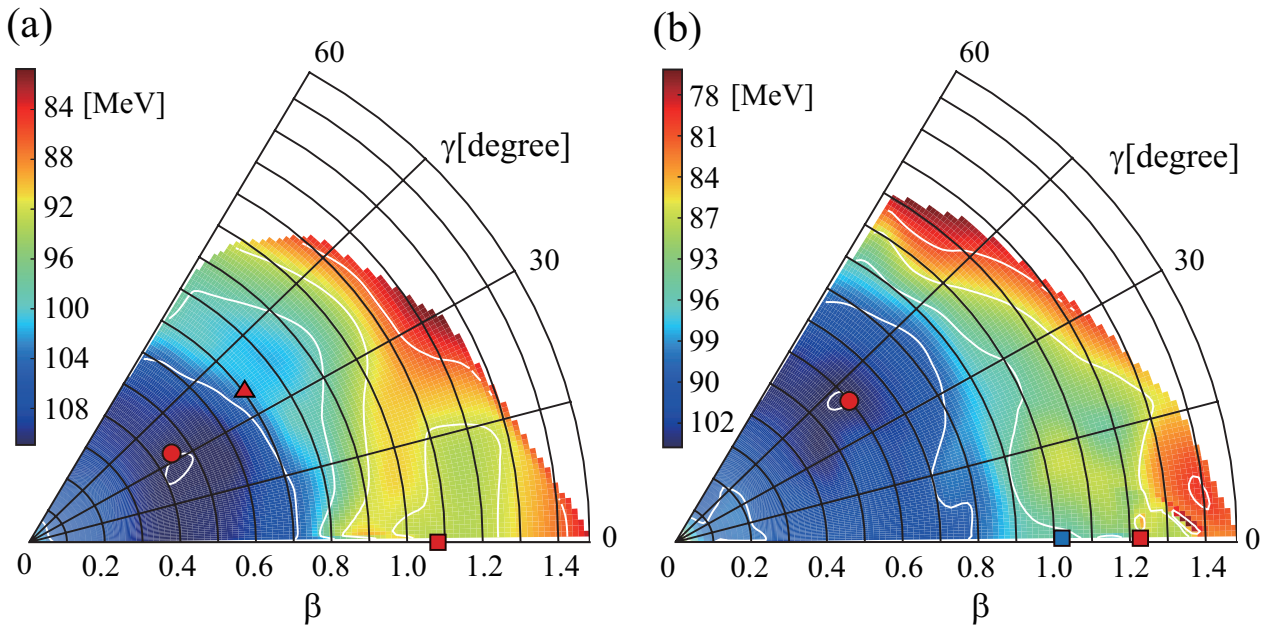

Figure 3.13: Angular momentum projected energy surfaces for (a) the $J^\pi = 0^+$ and (b) $J^\pi = 1^-$ states as functions of quadrupole deformation parameters β and γ. The filled circles, triangles and boxes in the panel (a) show the ground, triangular and linear-chain structures, while in the panel (b), the circle shows the position of the energy minimum and filled boxes show the linear-chain configurations.

In Fig. 3.13, the energy surfaces for $J^\pi = 0^+$ and $J^\pi = 1^-$ states are shown as the function of quadrupole deformation parameters β and γ. The circles on the energy surfaces show the position of the energy minima. First, we discuss three different structures on the energy surface of positive parity based on their intrinsic density distributions shown in Fig. 3.14.

The energy minimum of the 0^+ state is located at $(\beta, \gamma) = (0.45, 31°)$ with the binding energy of 110.5 MeV. The intrinsic density distribution at the minimum is shown in Figs. 3.14 (a)(b). These figures clearly shown that this structure has no outstanding clustering. Figs. 3.14 (c)(d) show a different structure which we call triangular configuration located around $(\beta, \gamma) = (0.70, 37°)$. The 3α cluster core forms triangle configuration as seen in the density distribution. Table 3.10 (c)(d) show that four valence neutrons occupy the $(sd)^4$ shell, indicating $2\hbar\omega$ excitation. However, because of its asymmetric shape, the valence proton orbits are an admixture of the positive- and negative-

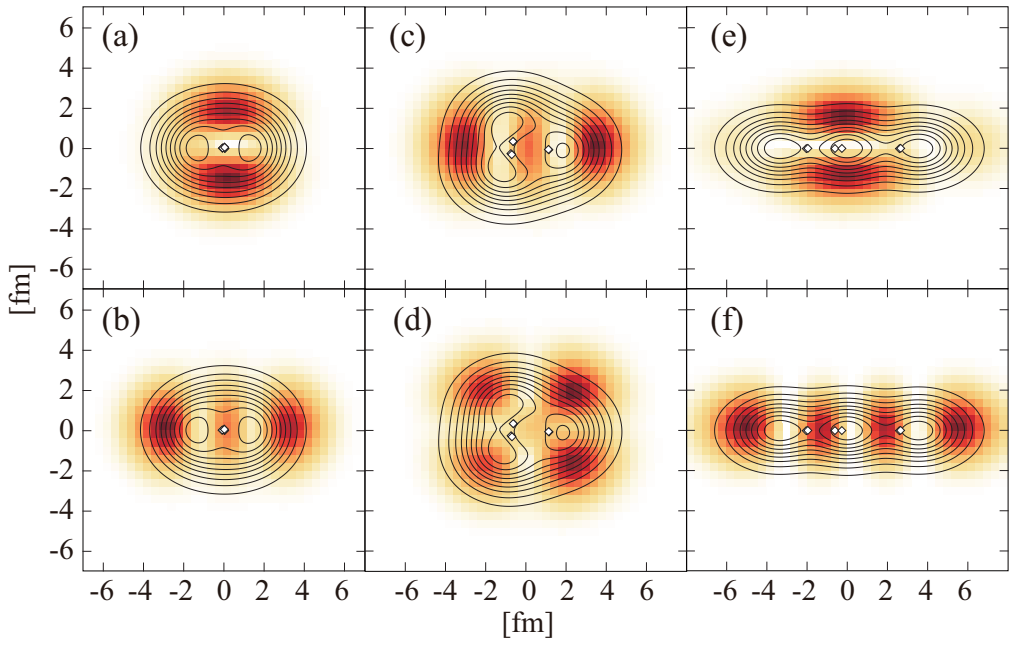

Figure 3.14: Density distributions of positive parity states of the ground (a)(b), triangular (c)(d), and linear-chain (e)(f) configurations. The contour lines show the proton density distributions. The color plots show the single-particle orbits occupied by four valence neutrons. The lower panels show the most weakly bound two neutrons, while the upper panels show the other two valence neutrons. Open boxes show the centroids of the Gaussian wave packets describing protons.

parity components. We note that a similar configuration appears in ^{14}C, which also have valence neutrons shown in the panel (c) but without those shown in the panel (d).

Further increase of the deformation realizes the linear-chain configuration in the strongly prolate deformed region. In this region, there is an energy plateau around the local energy minimum located at $(\beta, \gamma) = (1.08, 0^\circ)$. As seen in Fig. 3.14 (e)(f), its proton density distribution shows striking 3α cluster configuration with linear alignment. In addition, the properties of valence neutron orbits listed in Table 3.10 (e)(f) show that two valence neutrons occupy the π-orbit and the other two neutrons occupy the σ-orbit. Here the π-orbit in ^{16}C denotes $3/2^-_\pi$ and the σ-orbit denotes the $1/2^-_\sigma$ depending on the value of $|j_z|$ and parity. Therefore, with these definitions, this state is regarded to have the $(3/2^-_\pi)^2(1/2^-_\sigma)^2$ configuration.

The energy minimum of the energy surface for the 1^- states (Fig. 3.13 (b)) is located at $(\beta, \gamma) = (0.59, 40^\circ)$ with the binding energy of 103.6 MeV. At the minimum, the single-particle properties show the $1p1h$-configuration $\nu(p_{1/2})^{-1}(d_{5/2})^1$.

Table 3.10: Properties of the valence neutron orbit shown in Fig. 3.14. Each column shows the single-particle energy ε in MeV, the amount of the positive-parity component p^+ and the angular momenta defined by Eqs. (2.31)-(2.33).

	ε	p^+	j	$\lvert j_z\rvert$	l	$\lvert l_z\rvert$
(a)	-8.69	0.01	0.7	0.5	1.1	1.0
(b)	-3.95	0.99	2.2	0.5	1.8	0.4
(c)	-5.84	0.98	2.2	1.9	1.9	1.6
(d)	-2.97	0.98	2.4	1.9	2.1	1.8
(e)	-6.31	0.05	1.8	1.4	1.4	1.0
(f)	-3.16	0.07	2.8	0.6	2.6	0.3

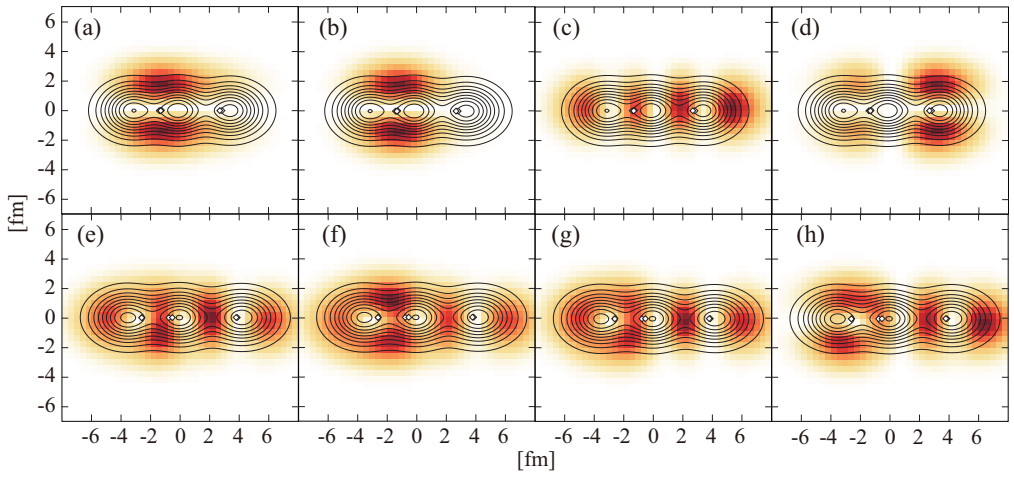

Figure 3.15: Density distributions of negative parity linear-chain states. The panels (a)-(d) correspond to the state at $(\beta, \gamma) = (1.02, 1^\circ)$, while the panels (e)-(h) correspond to the state at $(\beta, \gamma) = (1.23, 1^\circ)$. The contour lines show the proton density distributions. The color plots show the single-particle orbits occupied by four valence neutrons. The panels (a) and (e) show the most deeply bound valence neutrons, while the panels (d) and (h) show the most weakly bound neutrons. Open boxes show the centroids of the Gaussian wave packets describing protons.

Figs. 3.15 (a)-(d) show a basis wave function located at $(\beta, \gamma) = (1.02, 1^\circ)$ in Fig. 3.13(b). This linear-chain configuration appears in the prolate deformed region, although there is no plateau in the energy surface of negative parity. The density distribution and properties of valence neutron orbits show that the 3α core is linearly aligned and three valence neutrons (Figs. 3.15 (a)-(c)) occupy $(3/2^-_\pi)^2(1/2^-_\sigma)^1$ orbits similar to the linear-chain configuration of positive parity. However, the most weakly bound valence neutron (Fig. 3.15 (d)) occupies a different orbit. The properties of single-particle orbit (Table 3.11 (d)) show that the most weakly bound valence neutron occupies the *ungerade* π-orbit which is a linear-combination of ^{10}Be π-orbit with anti-phase as illustrated in Fig. 3.16. In addition, it can be seen that this $(3/2^+_\pi)$ orbit locates around α-particle of right side preferably. It is noted that this type of the linear-chain has not been found in ^{14}C. We consider that this orbit is unbound in ^{14}C, and makes the negative-parity linear-chain unstable in ^{14}C.

Figs. 3.15 (e)-(h) show another intrinsic wave function belonging the linear-chain configuration appeared around $(\beta, \gamma) = (1.23, 1^\circ)$. Although the density distribution and properties of valence neutron orbit do not show the clear molecular orbital nature because of the strong parity mixing, this intrinsic wave function has the largest overlap with member states of a linear-chain band as mentioned in next subsection.

Table 3.11: Properties of the valence neutron orbits shown in Fig. 3.15. Each column shows the single-particle energy ε in MeV, the amount of the positive-parity component p^+ and the angular momenta defined by Eqs. (2.31)-(2.33).

	ε	p^+	j	$\lvert j_z\rvert$	l	$\lvert l_z\rvert$
(a)	-6.76	0.05	2.1	1.5	1.7	1.0
(b)	-6.63	0.16	2.0	1.5	1.7	1.0
(c)	-2.10	0.03	2.7	0.5	2.5	0.3
(d)	-0.78	0.92	3.0	1.5	2.7	1.0
(e)	-4.80	0.08	2.6	1.1	2.3	0.7
(f)	-4.48	0.16	2.7	1.2	2.4	0.8
(g)	-4.07	0.23	2.8	1.0	2.6	0.6
(h)	-2.23	0.57	3.0	1.2	2.8	0.8

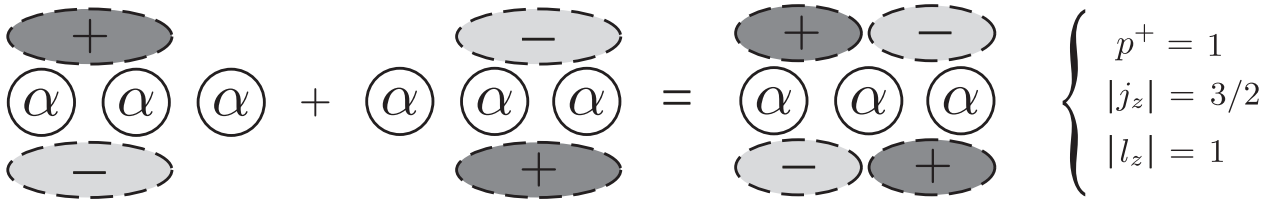

Figure 3.16: Schematic illustration of the *ungerade* π-orbit around the linear chain.

3.2.2 Energy spectrum

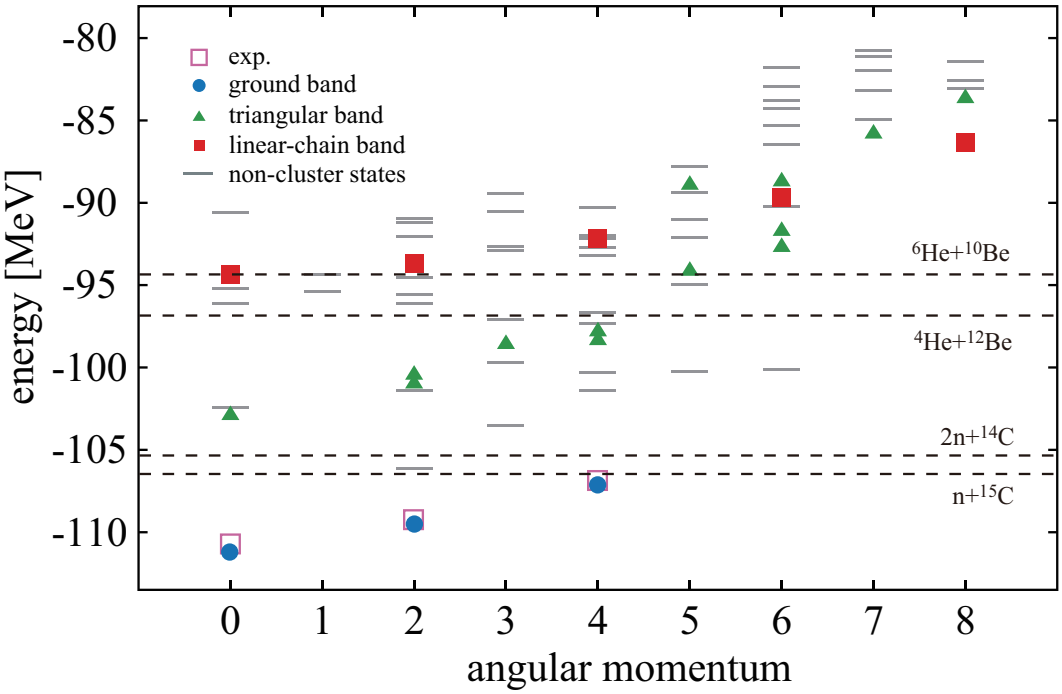

Figure 3.17: Positive-parity energy levels up to $J^\pi = 8^+$. Open boxes show the observed states with the definite spin-parity assignments, and other symbols show the calculated result. The filled circles, triangles and boxes show the ground, triangular and linear-chain bands, while lines show the non-cluster states which have reduced widths smaller than 0.10 MeV$^{1/2}$ except for the triangular band.

Figure 3.17 shows the spectrum of the positive-parity states obtained by the GCM calculation. The properties of the several selected states are listed in Table 3.12. For the positive parity, it is found that three different bands exist; ground, triangular and linear-chain bands. We classify the excited states which have α reduced widths larger than 0.10 MeV$^{1/2}$ at the channel radius $a = 6.0$ fm as cluster states. In these results, only the linear-chain band satisfies this condition. For the triangular configuration, the member states have overlap larger than 0.50 with the configuration shown in Fig. 3.14 (c)(d) are classified as the triangular band. The intra-band $B(E2)$ strengths are listed in Table 3.13.

The member states of the ground band are dominantly composed of the configurations around the energy minimum of the

Table 3.12: Excitation energies (MeV), α reduced widths (MeV$^{1/2}$), α-cluster and neutron spectroscopic factors of several selected positive-parity states. The reduced widths, α and neutron S-factors are calculated for the decays to the ground states of daughter nuclei.

Band	J^π	E_x	γ_α(6.0fm)	S_α	S_n
Ground	0^+_1	0.00	0.00	0.03	0.22
	2^+_1	1.69	0.00	0.00	0.35
	4^+_1	4.04	0.00	0.00	0.01
Triangular	0^+_2	8.35	0.01	0.05	0.12
	2^+_4	10.22	0.00	0.00	0.01
	2^+_5	10.79	0.00	0.01	0.02
Linear-chain	0^+_6	16.81	0.28	0.11	0.00
	2^+_9	17.51	0.23	0.07	0.00
	4^+_{10}	18.99	0.26	0.09	0.00
	6^+_5	21.49	0.23	0.07	0.00

energy surface. The ground state has the largest overlap (Eq. (2.27)) with the basis wave function shown in Fig. 3.14 (a)(b) that amounts to 0.98, and the calculated binding energy is 111.2 MeV which is close to the observed binding energy of 110.8 MeV. The excitation energies of other member states 2_1^+ and 4_1^+ are also reproduced well. This band has no outstanding clustering but has a shell model like structure with a $\nu(sd)^2$ configuration which can be confirmed from the small α-cluster spectroscopic factors and large neutron spectroscopic factors given in Table 3.12.

Because of its triaxial deformed shape, the triangular configuration generates two rotational bands built on the 0_2^+ and 2_5^+ states. The member states have overlap larger than 0.50 with the configuration shown in Fig. 3.14 (c)(d) which amount to, for example, 0.78 in the case of the 0_2^+ state. The member states with $J^\pi \geq 5^+$ are fragmented into several states because of the coupling with the non-cluster configurations. Compared to the linear-chain states, these bands have less pronounced clustering and α clusters are considerably distorted. As a result, the member states gain binding energy and the low-spin states are located well below the cluster thresholds. Because of the α-cluster distortion and deeper binding, the triangular configuration has small α spectroscopic factors and reduced widths as listed in Table 3.12.

Table 3.13: Calculated in-band $B(E2)$ strengths for the low-spin positive-parity states in units of $e^2\text{fm}^4$. The number in parenthesis is the observed data [98–102].

	$J_i \to J_f$	$B(E2; J_i \to J_f)$
Ground $\to$ Ground	$2_1^+ \to 0_1^+$	6.7 (0.92$\sim$4.2)
	$4_1^+ \to 2_1^+$	4.1
Triangular	$2_4^+ \to 0_2^+$	2.5
$\to$ Triangular	$2_5^+ \to 0_2^+$	0.9
	$3_3^+ \to 2_4^+$	9.5
	$3_3^+ \to 2_5^+$	8.5
Linear chain	$2_9^+ \to 0_6^+$	380.3
$\to$ Linear chain	$4_{10}^+ \to 2_9^+$	544.3
	$6_5^+ \to 4_{10}^+$	891.4

The linear-chain configuration generates a rotational band which built on the 0_6^+ state located at 16.8 MeV. The band-head 0_6^+ state has the largest overlap with the configuration shown in Fig. 3.14 (e)(f) that amounts to 0.94. The moment of inertia is estimated as $\hbar^2/2\Im$ =112 keV which is considerably larger than those of ground band ($\hbar^2/2\Im$ =196 keV) and triangular band ($\hbar^2/2\Im$ =238 keV). Owing to its large moment of inertia, the member state $J^\pi = 8^+$ located at $E_x = 24.8$ MeV becomes the yrast state. In addition, the large moment of inertia brings about the huge intra-band $B(E2)$ compared with those of ground and triangular bands as listed in Table 3.13. In contrast to the ground and triangular bands, the linear-chain band has the large α cluster spectroscopic factors and very small neutron spectroscopic factors. As all member states locate above the $\alpha + {}^{12}\text{Be}$ and ${}^6\text{He} + {}^{10}\text{Be}$ thresholds, the linear-chain states should decay into these two channels, which can be an important observable to identify the linear-chain state as discussed in the next subsection.

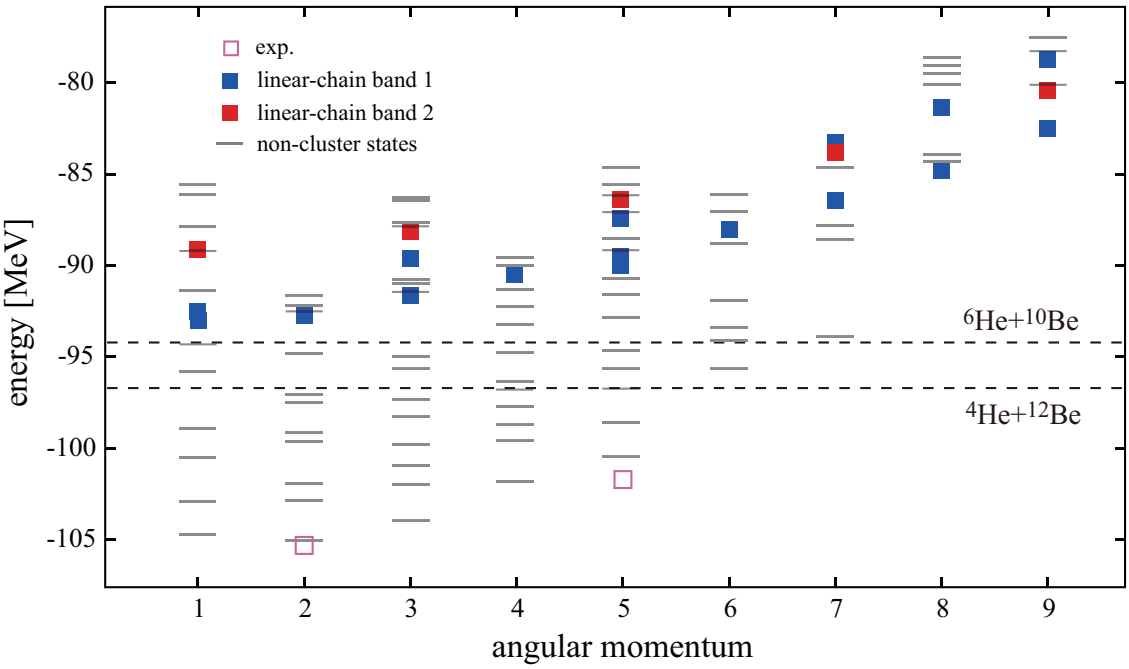

Figure 3.18: Negative-parity energy levels up to $J^\pi = 9^-$. Open boxes show the observed states with the definite spin-parity assignments [64, 103], and other symbols show the calculated result. The filled boxes show the linear-chain bands, while lines show the non-cluster states which have the reduced widths lower than 0.10 MeV$^{1/2}$.

Figure 3.18 shows the spectrum of the negative-parity states. Only two states (2^- and 5^-), which are described by open boxes in the figure, were observed with the definite spin-parity assignments [64, 103]. Our calculation shows the yrast band which is built on the 2^-_1 state located at 6.0 MeV, and the 2^-_1 and 5^-_1 member states of this rotational band are close to the observed two states. Since this band has the $1p1h$-configuration $\nu(p_{1/2})^{-1}(d_{5/2})^1$, the spectroscopic factors in the $[^{15}\mathrm{C}(g.s.) \otimes j]$ channels are negligibly small but those in the $[^{15}\mathrm{C}(1/2^-) \otimes d_{5/2}]$, $[^{15}\mathrm{C}(3/2^-) \otimes d_{5/2}]$, and $[^{15}\mathrm{C}(5/2^-) \otimes d_{5/2}]$ channels are large as listed in Table 3.14.

In the case of negative parity, the linear-chain configuration generates two different types of rotational bands. In the same manner to the positive-parity states, the excited states which have α reduced widths larger than 0.10 MeV$^{1/2}$ are classified as cluster states, and only linear-chain bands satisfy this condition. These bands are also located above the $\alpha + {}^{12}$Be and ^{6}He + ^{10}Be thresholds. This is in contrast to ^{14}C in which the linear-chain band is not obtained. The properties of the several selected linear-chain states are listed in Table 3.15 and $B(E2)$ strengths are listed in Table 3.16.

Table 3.14: Neutron spectroscopic factors of yrast band for negative-parity. The components of $^{15}\mathrm{C} \otimes s_{1/2}$ and $^{15}\mathrm{C} \otimes d_{3/2}$ are negligibly small.

	2^-_1	3^-_1	4^-_1	5^-_1
$^{15}\mathrm{C}(1/2^-) \otimes d_{5/2}$	0.03	0.42	-	-
$^{15}\mathrm{C}(3/2^-) \otimes d_{5/2}$	0.34	0.04	0.19	-
$^{15}\mathrm{C}(5/2^-) \otimes d_{5/2}$	0.67	0.07	0.48	0.27

Table 3.15: Excitation energies (MeV), α reduced widths (MeV$^{1/2}$), α-cluster spectroscopic factors of several selected states for negative parity. γ_α and S_α show the decay to the ground state (0_1^+) of ^{12}Be.

Band	J^π	E_x	γ_α(5.5fm)	γ_α(7.0fm)	S_α
Yrast band	2_1^-	6.11	-	-	-
	3_1^-	7.25	0.00	0.00	0.02
	4_1^-	9.34	-	-	-
	5_1^-	10.71	0.00	0.00	0.00
Linear-chain	1_7^-	18.28	0.04	0.00	0.01
band 1	1_8^-	18.64	0.02	0.01	0.00
	3_9^-	19.45	0.10	0.01	0.03
	3_{13}^-	21.57	0.05	0.02	0.01
Linear-chain	1_{11}^-	22.05	0.04	0.12	0.03
band 2	3_{14}^-	23.00	0.04	0.12	0.03
	5_{15}^-	24.76	0.03	0.11	0.02
	7_6^+	27.35	0.06	0.11	0.01

The first band, which we call the linear-chain band 1 (blue square), is dominantly composed of the wave function shown in Fig. 3.15 (a)-(d) although it is mixed with non-cluster configurations. Furthermore there is a mixing of $K = 0^-$ and 1^- components. As a result, the member states of this band are fragmented into several states. For example, we classify both of the 1_7^- and 1_8^- states as the member states of the band, whose overlaps with the basis wave functions shown in Fig. 3.15 (a)-(d) are 0.24 and 0.64, respectively. Because of the fragmentation, the intra-band $B(E2)$ values are smaller than those of positive-parity linear-chain band. However, the moment of inertia, $\hbar^2/2\Im$ =118 keV, is comparable with that of positive-parity linear chain. In this band, the neutron spectroscopic factors are negligible. Compared with the positive-parity linear chain, α spectroscopic factors are small, but sufficiently larger than other negative-parity states.

The other band, the linear-chain band 2 (red square), is built on the 1_{11}^- state at $E_x = 22.1$ MeV which is about 3.6 MeV higher than the linear-chain band 1. The 1_{11}^- state has the largest overlap with the wave function shown in Fig. 3.15 (e)-(h) which amounts to 0.92. In contrast to the linear-chain band 1, the member states of this band have the $K = 0$ quantum number and clearly form a single rotational band. In addition, the moment of inertia, $\hbar^2/2\Im$ =98 keV, and the intra-band $B(E2)$ values are as large as those of positive-parity linear-chain band. As well as the linear-chain band 1, the neutron spectroscopic factors are negligible while the α spectroscopic factors are a bit larger but smaller than those of positive-parity linear-chain band.

Table 3.16: Calculated in-band $B(E2)$ strengths for the low-spin negative-parity states in units of e^2fm^4.

	$J_i \to J_f$	$B(E2; J_i \to J_f)$
Linear-chain band 1	$2_9^- \to 1_7^-$	53.2
	$2_9^- \to 1_8^-$	25.0
	$3_9^- \to 2_9^-$	37.7
	$3_{13}^- \to 2_9^-$	0.1
	$4_{11}^- \to 3_9^-$	72.0
	$4_{11}^- \to 3_{13}^-$	4.0
Linear-chain band 2	$3_{14}^- \to 1_{11}^-$	492.2
	$5_{15}^- \to 3_{14}^-$	561.6
	$7_6^- \to 5_{15}^-$	556.1

3.2.3 Decay mode

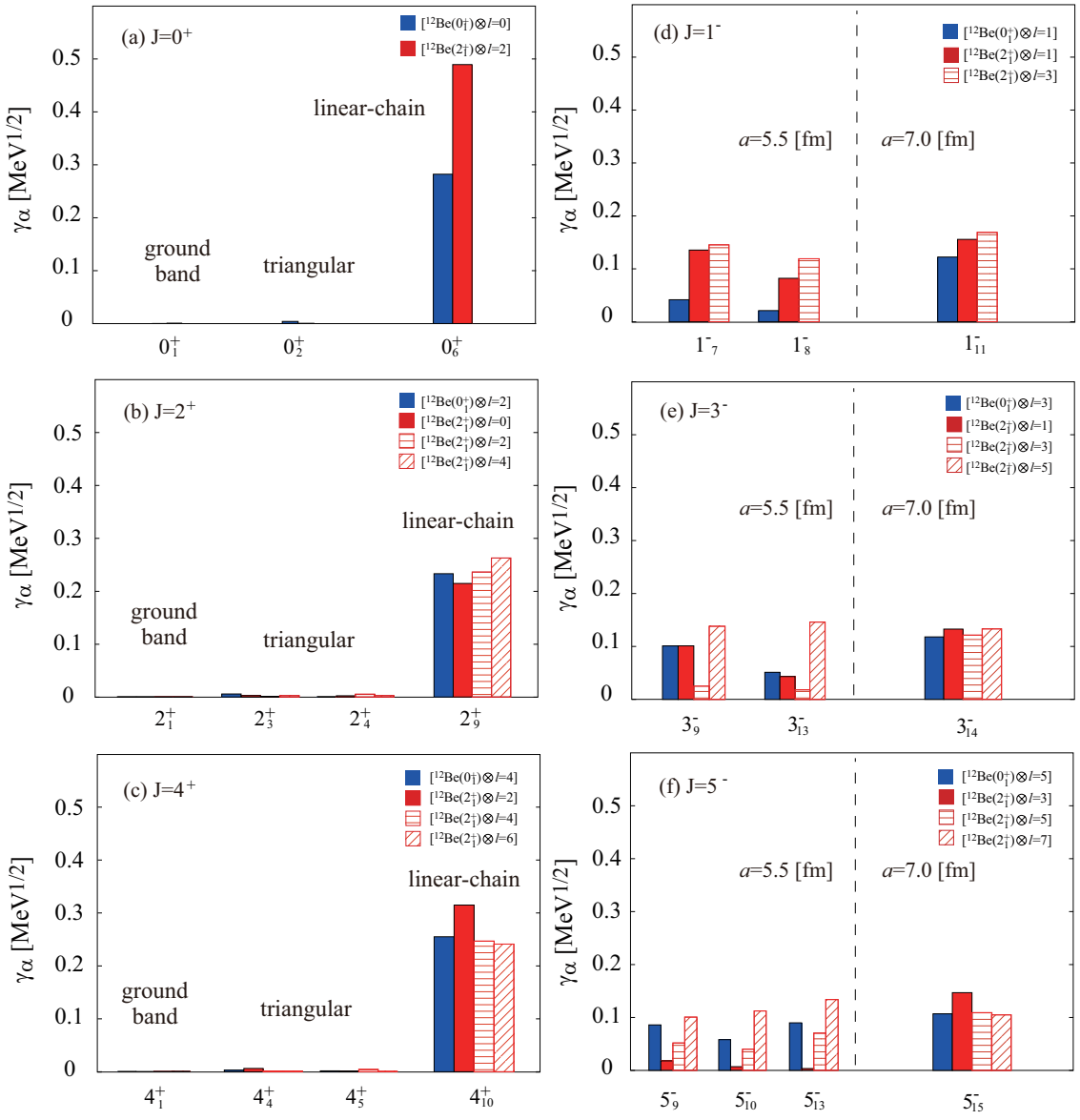

Figure 3.19: Calculated α-decay reduced widths. Panels (a)-(c) show the decay of the positive-parity states to the ground band of ^{12}Be. Panels (d)-(f) show the decay of the negative-parity states to the ground band of ^{12}Be. The channel radii a are 6.0 fm for (a)-(c) and 5.5(left side), 7.0(right side) fm for (d)-(f), respectively.

Figure 3.19 shows the α reduced widths of several selected low-spin states. For positive parity, we show the member states of the ground, triangular and linear-chain bands, while for the negative parity, we show only the states which have reduced widths larger than 0.1 MeV$^{1/2}$. The decay channels are indicated as $[^{12}\mathrm{Be}(j^\pi) \otimes l]$ where j^π and l denote the angular momentum of the ^{12}Be ground band and the relative angular momentum between ^{12}Be and α-particles, respectively. Here, ^{12}Be is assumed to have two neutrons in π-orbit and the other two neutrons in σ-orbit. The channel radii a are 6.0 fm for (a)-(c) and 5.5(left side), 7.0(right side) fm for (d)-(f), which are chosen to be smoothly connected to the Coulomb wave function. The detailed values of α and ^{6}He decay widths for linear-chain states are listed in Table 3.17.

Table 3.17: Partial decay widths (keV) of linear-chain bands for (a) positive-parity and (b) negative-parity linear-chain band 2. The channel radii a are (a) 6.0 fm and (b) 7.0 fm, respectively.

(a) Positive parity					
J^π	E_x	$\Gamma_\alpha(^{12}\mathrm{Be}(0_1^+))$	$\Gamma_\alpha(^{12}\mathrm{Be}(2_1^+))$	$\Gamma_{^6\mathrm{He}}(^{10}\mathrm{Be}(0_1^+))$	$\Gamma_{^6\mathrm{He}}(^{10}\mathrm{Be}(2_1^+))$
0_6^+	16.81	335	1	-	-
2_9^+	17.51	300	118	0	-
4_{10}^+	18.99	505	954	33	-
6_5^+	21.49	535	1591	78	18
(b) Negative parity					
1_{11}^-	22.05	198	567	77	63
3_{14}^-	23.00	196	597	84	115
5_{15}^-	24.76	181	615	92	173
7_6^-	27.35	224	763	100	225

In the positive parity, the linear-chain band (the 0_6^+, 2_9^+, and 4_{10}^+ states) has large reduced widths compared to the ground and the triangular bands. It is also noted that the α reduced widths of other excited states are also much smaller than the linear-chain band. Hence, in the calculated energy region, the linear chain band has the largest reduced widths. Another point to be noted is the decay pattern of the linear-chain band. The reduced widths in the $[^{12}\mathrm{Be}(2_1^+) \otimes l]$ channels are as large as or even larger than those in the $[^{12}\mathrm{Be}(0_1^+) \otimes l]$ channel. This dominance of the $^{12}\mathrm{Be}(2_1^+)$ component in the linear-chain band is owed to the strong angular correlation between α clusters which is brought about by their linear alignment. This property is in contrast to the Hoyle state where α-particles are mutually orbiting with $l = 0$, and hence, the $^8\mathrm{Be}(0_1^+)$ component dominates [15]. Similar properties of the linear-chain configuration was also discussed in ^{12}C [91] and ^{14}C. Therefore, if the decay to $^{12}\mathrm{Be}(2_1^+)$ is confirmed, it will be a strong evidence for the linear-chain formation.

Figure 3.20 shows the ^{6}He reduced widths of linear-chain states for positive parity. We calculated the ^{6}He reduced widths for both $^6\mathrm{He} + ^{10}\mathrm{Be}(0_1^+, 2_1^+)$ and $^6\mathrm{He} + ^{10}\mathrm{Be}(0_2^+, 2_3^+)$ channels. Here we assumed that the ground band of $^{10}\mathrm{Be}(0_1^+$ and $2_1^+)$ has the π-orbit neutrons, while the excited state (0_2^+, 2_3^+, and so on) of ^{10}Be has the σ-orbit neutrons. Fig. 3.20(a) corresponds to the decay to $^6\mathrm{He} + ^{10}\mathrm{Be}(0_1^+, 2_1^+)$ and the panel (b) corresponds to the decay to $^6\mathrm{He} + ^{10}\mathrm{Be}(0_2^+, 2_3^+)$, respectively. Although the magnitudes of the ^{6}He reduced widths are about a factor of 2 smaller than that of α reduced widths, they are still sufficiently large compared to any other excited states. It is also noted that the magnitudes of $^6\mathrm{He} + ^{10}\mathrm{Be}(0_1^+, 2_1^+)$ and $^6\mathrm{He} + ^{10}\mathrm{Be}(0_2^+, 2_3^+)$ reduced widths are almost of the same order. This is caused by the unique configuration of linear-chain state in ^{16}C. The linear-chain configuration in ^{16}C has the two π-orbit neutrons and two σ-orbit neutrons, hence, the linear-chain configuration of ^{16}C can decay into both $^{10}\mathrm{Be}(0_1^+, 2_1^+)$ and $^{10}\mathrm{Be}(0_2^+, 2_3^+)$. The results shown in Fig. 3.20 are consistent with this explanation. This decay property should be compared with that of the linear-chains in ^{14}C. As already discussed in previous subsection, the π-bond linear-chain state of ^{14}C decays into the $^{10}\mathrm{Be}(0_1^+, 2_1^+)$ dominantly, while the decay to $^{10}\mathrm{Be}(0_2^+, 2_3^+)$ is suppressed. In contrast to the π-bond linear-chain, the σ-bond linear-chain state of ^{14}C decays into the $^{10}\mathrm{Be}(0_2^+, 2_3^+)$ dominantly and the decay to $^{10}\mathrm{Be}(0_2^+, 2_3^+)$ is suppressed.

For the negative parity, it can be seen that the linear-chain band 1 and 2 show relatively smaller reduced widths compared to the positive-parity linear-chain band. The linear-chain configurations of negative parity do not match the $\alpha + ^{12}\mathrm{Be}(0_1^+, 2_1^+)$ configuration because of the existence of

the valence neutron which occupies the *ungerade* $(3/2^+_\pi)$ (see Fig. 3.15). Therefore, the decay to the $\alpha + {}^{12}\mathrm{Be}(0^+_1, 2^+_1)$ channel is suppressed. The characteristic decay patterns of the linear-chain configuration can be also seen in negative parity, namely, the reduced widths in the $[{}^{12}\mathrm{Be}(2^+_1) \otimes l]$ channels are larger than $[{}^{12}\mathrm{Be}(0^+_1) \otimes l]$ channels. In addition, the partial decay widths of the linear-chain band 2 listed in Table 3.17 (b) are very large because of their high excitation energies. Therefore, if it is observed, the linear-chain formation in the negative parity can be supported strongly. However, it is not easy to distinguish the linear-chain band 1 and 2 from α reduced widths because they are almost of the same magnitude.

Figure. 3.21 shows the ${}^6\mathrm{He}$ reduced widths of negative-parity linear-chain states for both ${}^{10}\mathrm{Be}(0^+_1, 2^+_1)$ and ${}^{10}\mathrm{Be}(0^+_2, 2^+_3)$ channels. It is interesting that a characteristic difference between the linear-chain band 1 and 2 appears in the ${}^6\mathrm{He}$ reduced widths. The linear-chain band 2 has the same magnitude of the ${}^6\mathrm{He}$ reduced widths as the α reduced widths. In addition, the ${}^6\mathrm{He}$ reduced widths of the linear-chain band 2 are even larger than those of positive-parity linear-chain band (see Fig.3.20). On the other hand, the linear-chain band 1 has the smaller ${}^6\mathrm{He}$ reduced widths, especially as it rarely decays into ${}^6\mathrm{He} + {}^{10}\mathrm{Be}(0^+_2, 2^+_3)$. This characteristic difference enables to distinguish the linear-chain bands 1 and 2.

A high-lying excited state at 20.6 MeV was observed by the breakup of ${}^6\mathrm{He} + {}^{10}\mathrm{Be}$ [74]. Since its spin-parity has not been assigned, several calculated excited states can be the candidate for the observed high-lying state, including the linear-chain states naturally. However, the positive- or negative-parity linear-chain states only show the large ${}^6\mathrm{He}$ reduced widths near 20.6 MeV. Although further experimental studies are needed, we suggest the linear-chain state as the candidate for the observed high-lying state.

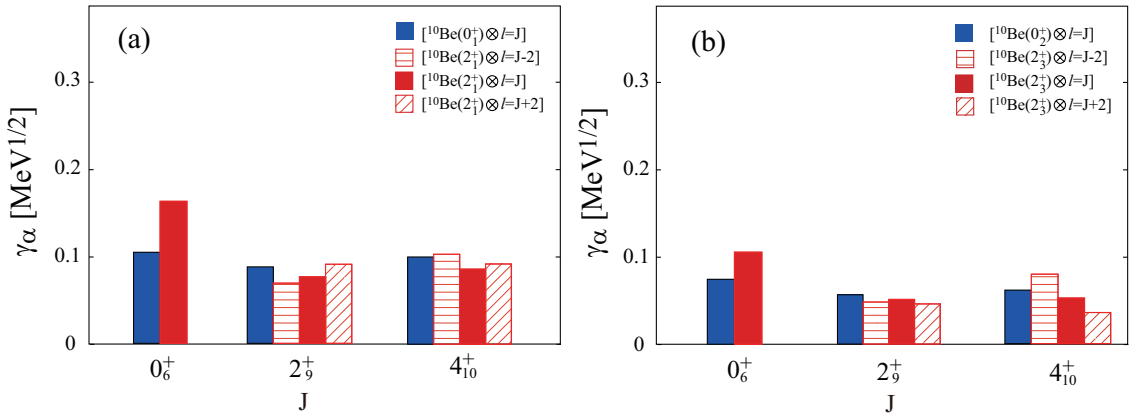

Figure 3.20: Calculated ${}^6\mathrm{He}$-decay reduced widths of linear-chain states in positive parity. The panel (a) shows the decay into the ground band of ${}^{10}\mathrm{Be}$. The panel (b) shows the decay into the excited band of ${}^{10}\mathrm{Be}$. The channel radius a is 6.0 fm.

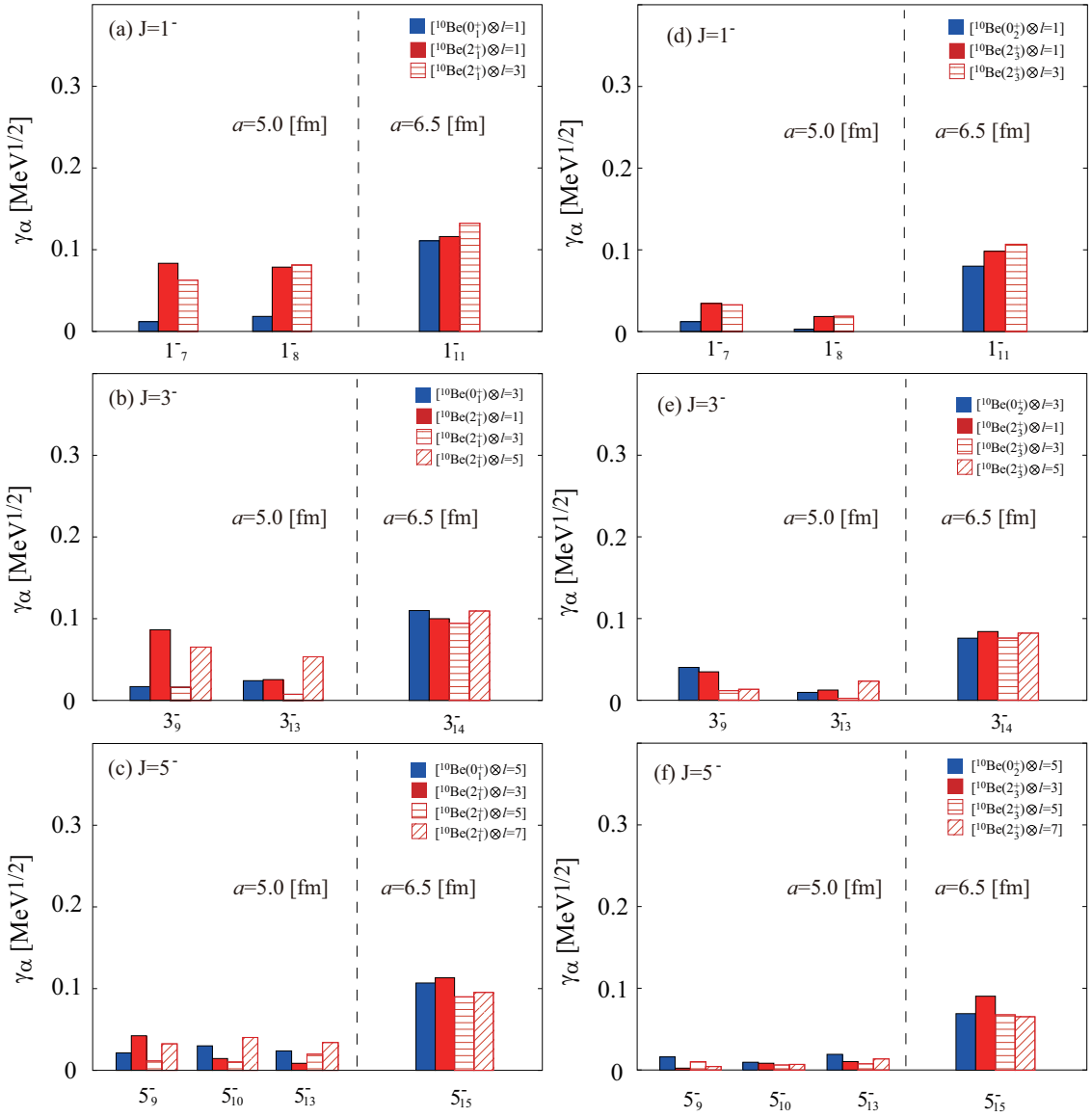

Figure 3.21: Calculated ^{6}He-decay reduced widths of linear-chain states in negative parity. Panels (a)-(c) show the decay into the ground band of ^{10}Be. Panels (d)-(f) show the decay into the excited band of ^{10}Be.

Chapter 4

Summary

To investigate the existence of the linear-chain state, we study the excited states of ^{14}C and ^{16}C based on the AMD calculation.

In the positive-parity states of ^{14}C, it is found that three different configurations appear depending on the magnitude of the deformation and the valence neutron configurations. At oblate deformed region, the triangular configuration of 3α cluster is obtained, while at strong deformed prolate region, two different linear-chain configurations with valence neutrons in π-orbit and σ-orbit are obtained.

These cluster configurations generate clear rotational bands. The π-bond linear chain generates a rotational band around the α threshold energy, while triangular and σ-bond linear chain generate rotational bands well below and well above the threshold, respectively. The energies, moment of inertia and α-decay widths of the π-bond linear chain are in reasonable agreement with the resonances observed by the $\alpha+^{10}$Be. Thus, the π-bond linear-chain formation in ^{14}C looks plausible. Furthermore, the calculation predicts that the π-bond linear-chain also decays to the ^{10}Be(2^+_1) as well as to the ^{10}Be(0^+_1). This characteristic decay pattern is, if measured, another evidence of the linear-chain formation.

On the other hand, the σ-bond linear-chain generates a rotational band around the ^{6}He threshold energy which is 7.5 MeV higher than the α threshold energy. Newly observed resonance states are close to energies of both the low-spin states of the σ-bond linear-chain and the 6^+ state of the π-bond linear-chain. In order to distinguish the π- and σ-bond linear-chain, We focus on the decay patterns of them. Reduced widths show that the π-bond linear-chain states decay into the ground band of ^{10}Be, while the σ-bond linear-chain states decay into the excited band of ^{10}Be. This difference is due to the molecular orbit of ^{10}Be. From ^{6}He reduced width, in addition, it is found that the σ-bond linear-chain states decay into not only the excited band of ^{10}Be but also $^6\mathrm{He}+\alpha+\alpha$. Similarly to ^{10}Be, the calculation predicts that the σ-bond linear-chain states decays to the ^{8}Be(2^+) as well as to the ground state of ^{8}Be. Therefore, this three-body decay can be also a additional signature of the σ-bond linear-chain formation.

We also discuss the energy shift of the linear-chain states in ^{14}C-^{14}O. In ^{14}O, we find three types of cluster configuration, the triangular, π-bond linear-chain, and σ-bond linear-chain, which is already mentioned in ^{14}C. The energy shift is negligibly small for the π-bond linear-chain while it is prominent for the σ-bond linear chain. The large energy difference of the σ-bond linear-chain can be accounted for in terms of the reduction in the Coulomb energy associated with the spatially extent of the σ-orbit. This result is supported by the large radius of the single-particle orbit and the reduction of the Coulomb energy of the σ-orbit. Therefore, the Thomas-Ehrman shift can bee seen clearly in the σ-bond linear chain. The same character is also seen in the mirror pair of ^{10}Be-^{10}C.

In the negative-parity states of ^{14}C, the negative-parity partners of the cluster states are also obtained by the energy variation. However, because of the mixing with the non-cluster configura-

tions, these cluster configurations do not correspond to a single eigenstate in excited states. As a result, many excited states that have sizable α reduced width are obtained, and it makes the correspondence between the theory and experiment ambiguous. Thus, the present result does not show the linear-chain formation in the negative parity, although further studies are in need to identify the structure of the observed negative-parity resonances.

In the positive-parity states of ^{16}C, it is shown that the linear-chain configuration has the valence neutrons occupying molecular orbits $(3/2^-_\pi)^2(1/2^-_\sigma)^2$. It generates a rotational band built on the 0^+ state at 16.8 MeV and its moment of inertia is estimated as $\hbar^2/2\Im$ =112 keV. It is shown that the linear-chain states have the large α and ^{6}He reduced widths. In particular, the large α reduced widths in the $\alpha + {}^{12}\mathrm{Be}(2^+_1)$ channel is a strong evidence for the linear-chain configuration. In the case of the ^{6}He decay, the magnitudes of the reduced decay widths in both $^{10}\mathrm{Be}(0^+_1, 2^+_1)$ and $^{10}\mathrm{Be}(0^+_2, 2^+_3)$ channels are almost of the same order. Compared with ^{14}C, this is caused by the unique configuration of the linear chain in ^{16}C.

In the negative-parity states of ^{16}C, is is found that two types of linear-chain bands exist. The first band, which we call the linear-chain band 1, is composed of the linear-chain configuration with the $(3/2^-_\pi)^2(1/2^-_\sigma)(3/2^+_\pi)$ molecular orbits. This band is built on 1^- states located around 18.5 MeV. Because of the mixing with non-cluster states and the mixing of $K = 0^-$ and 1^- components, the member states are fragmented into several states. The other band, which we call the linear-chain band 2, is built on 1^- states located around 22.1 MeV. Although this band does not have the clear molecular orbital configuration, the single rotational $K = 0$ band is clearly formed with the large moment of inertia $\hbar^2/2\Im$ =98 keV. The α reduced widths of these two linear-chains are smaller than those of positive-parity linear-chain band, but are sufficiently large to be distinguished from other non-cluster states. These two linear chains cannot be distinguished based on the α reduced widths because they are almost same magnitude. However, the ^{6}He reduced widths of the linear-chain band 2 are larger than those of linear-chain band 1. We conclude that this characteristic difference enables to distinguish the linear-chain bands 1 and 2.

In conclusion, the present study has provided the significant progress for the establish of the linear-chain formation in carbon isotopes although it must be emphasized that further experimental studies are in need to resolve the inconsistency between the data and to firmly establish the linear-chain formation. More neutron-rich carbon isotopes serve more interests us because the valence neutrons in such isotopes need to occupy the higher molecular orbits in the linear-chain configuration. Therefore, we consider that we can find new types of the molecular orbit in the linear-chain states of ^{18}C and ^{20}C. In addition, it has not been yet clarified that the 4α linear-chain formation appears in oxygen isotopes. It is very important to get a deep insight into how heavy the linear chain can exist.

Chapter 5

Acknowledgements

The author would like to thank Dr. M. Kimura for the fruitful discussions. Also, the author has had the support and encouragement of Mr. S. Koyama, Dr. H. Ohtsu, Dr. J. Li, and Prof. Y. L. Ye. The author thanks Dr. Y. Chiba for helps in the numerical calculation and also the members of the nuclear theoretical group at Hokkaido University for warm encouragement. This work was supported by JSPS KAKENHI Grant No. 16J04889.

Bibliography

[1] M. G. Mayer, Phys. Rev. **75**, 1969 (1949).

[2] J. A. Wheeler, Phys. Rev. **52**, 1107 (1937).

[3] F. Hoyle, Astrophys. J. Suppl. Ser. **1**, 121 (1954).

[4] C. W. Cook *et al.*, Phys. Rev. **107**, 508 (1957).

[5] P. Navratil, J.P. Vary, and B.R. Barrett, Phys. Rev. Lett. **84**, 5728 (2000).

[6] E. Uegaki, S. Okabe, Y. Abe, and H. Tanaka, Prog. Theor. Phys. **57**, 1262 (1977); *ibid.* **62**, 1621 (1979).

[7] M. Kamimura, Nucl. Phys. A **351**, 456 (1981).

[8] Y. Fujiwara, H. Horiuchi, K. Ikeda, M. Kamimura, K. Kato, Y. Suzuki, and E. Uegaki, Suppl. Prog. Theor. Phys. **68**, 29 (1980).

[9] P. Descouvemont and D. Baye, Phys. Rev. C **36**, 54 (1987).

[10] A. Tohsaki, H. Horiuchi, P. Schuck, and G. Röpke, Phys. Rev. Lett. **87**, 192501 (2001).

[11] Y. Funaki, A. Tohsaki, H. Horiuchi, P. Schuck, and G. Röpke, Phys. Rev. C **67**, 051306(R) (2003).

[12] M. Chernykh *et al.*, Phys. Rev. Lett. **98**, 032501 (2007).

[13] Y. Kanada-En'yo, Phys. Rev. Lett. **81**, 5291 (1998).

[14] E. Epelbaum *et al.*, Phys. Rev. Lett. **109**, 252501 (2012).

[15] Y. Funaki, H. Horiuchi, and A. Tohsaki, Prog. Part. Nucl. Phys. **82** 78-132 (2015).

[16] Y. Funaki, Phys. Rev. C **94**, 024344 (2016).

[17] M. Itoh *et al.*, Nucl. Phys. A **738**, 268 (2004).

[18] M. Itoh *et al.*, Phys. Rev. C **84**, 054308 (2011).

[19] D. J. Marín-Lámbarri *et al.*, Phys. Rev. Lett. **113**, 012502 (2014).

[20] H. Horiuchi and K. Ikeda, Prog. Theor. Phys. **40**, 277 (1968).

[21] M. Libert-Heinemann *et al.*, Nucl. Phys. A **339**, 429 (1980).

[22] Y. Funaki, T. Yamada, A. Tohsaki, H. Horiuchi, G. Röpke, and P. Schuck, Phys. Rev. C **82**, 024312 (2010).

[23] Y. Kanada-En'yo, Phys. Rev. C **89**, 024302 (2014).

[24] M. Freer, Rep. Prog. Phys. **70**, 2149 (2007).

[25] K. Wildermuth and Th. Kanellopoulos, Nucl. Phys. **7**, 150 (1958); *ibid.* **9**, 449 (1958/59).

[26] R. K. Sheline and K. Wildermuth, Nucl. Phys **21**, 196 (1960).

[27] Y. Abe, *et al.*, Prog. Theor. Phys. Suppl. **68** (1980).

[28] H. Horiuchi, K. Ikeda, and K. Kato, Prog. Theor. Phys. Suppl. **192** (2012).

[29] K. Ikeda *et al.*, Prog. Theor. Phys. Suppl. **E68**, 464 (1968).

[30] H. Morinaga, Phys. Rev. **101**, 254 (1956).

[31] C. Kurokawa and K. Kato, Phys. Rev. C **71**, 021301(R) (2005).

[32] C. Kurokawa and K. Kato, Nucl. Phys. A **792**, 87 (2007).

[33] Y. Kanada-En'yo, Prog. Theor. Phys. **117**, 655 (2007).

[34] T. Suhara and Y. Kanada En'yo, Prog. Theor. Phys. **123**, 303 (2010).

[35] T. Neff and H. Feldmeier, Nucl. Phys. A **738**, 357 (2004).

[36] P. Chevallier *et al.*, Phys. Rev. **160**, 827 (1967).

[37] H. Horiuchi, K. Ikeda, and Y. Suzuki, Prog. Theor. Phys. Suppl. **52**, 89 (1972).

[38] W. von Oertzen, M. Freer, and Y. Kanada-En'yo, Phys. Rep. **432**, 43 (2006).

[39] D. L. Powell, G. M. Crawley, B. V. N. Rao, and B. A. Robson, Nucl. Phys. A **147**, 65 (1970).

[40] M. Seya, M. Kohno, and S. Nagata, Prog. Theor. Phys. **65**, 204 (1981).

[41] W. von Oertzen, Z. Phys. A **354**, 37 (1996); *ibid.* **357**, 355 (1997).

[42] Y. Kanada-En'yo, H. Horiuchi, and A. Dote, Phys. Rev. C **60**, 064304 (1999).

[43] N. Itagaki and S. Okabe, Phys. Rev. C **61**, 044306 (2000).

[44] N. Itagaki, S. Hirose, T. Otsuka, S. Okabe, and K. Ikeda, Phys. Rev. C **65**, 044302 (2002).

[45] Y. Kanada-En'yo, M. Kimura, and H. Horiuchi, C. R. Physique **4**, 497 (2003).

[46] M. Ito, Phys. Rev. C **85**, 044308 (2012).

[47] Y. Kanada-En'yo, Phys. Rev. C **91**, 014315 (2015).

[48] M. Freer *et al.*, Phys. Rev. Lett. **82**, 1383 (1999).

[49] Z. H. Yang *et al.*, Phys. Rev. Lett. **112**, 162501 (2014).

[50] M. Ito, N. Itagaki, H. Sakurai, and K. Ikeda, Phys. Rev. Lett. **100**, 182502 (2008).

[51] N. Itagaki, S. Okabe, K. Ikeda, and I. Tanihata, Phys. Rev. C **64**, 014301 (2001).

[52] W. von Oertzen and H. G. Bohlen, C. R. Physique **4**, 465 (2003).

[53] W. von Oertzen, *et al.*, Eur. Phys. J. A **21**, 193 (2004).

[54] N. Itagaki, W. von Oertzen, and S. Okabe, Phys. Rev. C **74**, 067304 (2006).

[55] T. Suhara and Y. Kanada-En'yo, Phys. Rev. C **82**, 044301 (2010).

[56] T. Suhara and Y. Kanada-En'yo, Phys. Rev. C **84**, 024328 (2011).

[57] J. Maruhn, N. Loebl, N. Itagaki, and M. Kimura, Nucl. Phys. A **833**, 1 (2010).

[58] N. Furutachi and M. Kimura, Phys. Rev. C **83**, 021303(R) (2011).

[59] T. Suhara, Y. Funaki, B. Zhou, H. Horiuchi, and A. Tohsaki, Phys. Rev. Lett. **112**, 062501 (2014).

[60] T. Baba, Y. Chiba, and M. Kimura, Phys. Rev. C **90**, 064319 (2014).

[61] P.W. Zhao, N. Itagaki, and J. Meng, Phys. Rev. Lett. **115**, 022501 (2015).

[62] B. J. Greenhalgh, *et al.*, Phys. Rev. C **66**, 027302 (2002).

[63] N. Soic, *et al.*, Phys. Rev. C **68**, 014321 (2003).

[64] H. G. Bohlen, *et al.*, Phys. Rev. C **68**, 054606 (2003).

[65] M. Milin, *et al.*, Nucl. Phys. A **730**, 285 (2004).

[66] N. I. Ashwood, *et al.*, Phsy. Rev. C **70**, 064607 (2004).

[67] D. L. Price *et al.*, Phys. Rev. C **75**, 014305 (2007).

[68] P.J. Haigh *et al.*, Phys. Rev. C **78**, 014319 (2008).

[69] M. Freer *et al.*, Phys. Rev. C **90**, 054324 (2014).

[70] A. Fritsch *et al.*, Phys. Rev. C **93**, 014321 (2016).

[71] H. Yamaguchi *et al.*, Phys. Lett. B **766**, 11 (2017).

[72] Z. Y. Tian *et al.*, Chinese Phys. C **40**, 111001 (2016).

[73] J. Li *et al.*, Phys. Rev. C **95**, 021303 (2017).

[74] D. Dell'Aquila *et al.*, Phys. Rev. C **93**, 024611 (2016).

[75] A. Volkov, Nucl. Phys. **74**, 33 (1965).

[76] N. Itagaki, T. Otsuka, K. Ikeda, and S. Okabe, Phys. Rev. Lett **92**, 142501 (2004).

[77] J. F. Berger, M. Girod, and D. Gogny, Comput. Phys. Comm. **63**, 365 (1991).

[78] Y. Kanada-En'yo, M. Kimura, and A. Ono, Prog. Theor. Exp. Phys. **2012**, 01A202 (2012).

[79] M. Kimura, T. Suhara, and Y. Kanada-En'yo, Eur. Phys. J. A **52**, 373 (2016).

[80] J. Decharge and D. Gogny, Phys. Rev. C **21**, 1568 (1980).

[81] M. Kimura, Phys. Rev. C **69**, 044319 (2004).

[82] Y. Kanada-En'yo and H. Horiuchi, Prog. Theor. Phys. **93**, 115 (1995).

[83] R. E. Peierls and J. Yoccoz, Proc. Phys. Soc. **70**, 381 (1957).

[84] J. J. Griffin and J. A. Wheeler, Phys. Rev. **108**, 311 (1957).

[85] D. L. Hill and J. A. Wheeler, Phys. Rev. **89**, 1102 (1953).

[86] Y. Kanada-En'yo, T. Suhara, and Y. Taniguchi, Prog. Theor. Exp. Phys. **2014**, 073D02 (2014).

[87] Y. Chiba and M. Kimura, Prog. Theor. Exp. Phys. **2017**, 053D01 (2017).

[88] F. Ajzenberg-Selove, Nucl. Phys. A **523**, 1 (1991).

[89] I. Angelia and K. P. Marinovab, At. Data Nucl. Data Tables **99**, 69 (2013).

[90] S. Raman, C. W. Nestor Jr., and P. Tikkanen, At. Data Nucl. Data Tables **78**, 1 (2001).

[91] Y. Suzuki, H. Horiuchi, and K. Ikeda, Prog. Theor. Phys. **47**, 5 (1972).

[92] R. G. Thomas, Phys. Rev. **88**, 1109 (1952).

[93] J.B. Ehrman, Phys. Rev. **81**, 412 (1951).

[94] L. V. Grigorenko, I. G. Mukha, I. J. Thompson, and M .V. Zhukov, Phys. Rev. Lett. **88**, 042502 (2002).

[95] E. Garrido, D. V. Fedorov, and A. S. Jensen, Phys. Rev. C **69**, 024002 (2004).

[96] L. V. Grigorenko, T. A. Golubkova, and M .V. Zhukov, Phys. Rev. C **91**, 024325 (2015).

[97] M. Ito, EPJ. Conf. **117**, 06014 (2016).

[98] N. Imai *et al.*, Phys. Rev. Lett. **92**, 062501 (2004).

[99] H. J. Ong *et al.*, Phys. Rev. C **73**, 024610 (2006).

[100] H. J. Ong *et al.*, Phys. Rev. C **78**, 014308 (2008).

[101] M. Wiedeking, *et al.*, Phys. Rev. Lett. **100**, 152501 (2008).

[102] M. Petri, *et al.*, Phys. Rev. C **86**, 044329 (2012).

[103] Y. Satou, *et al.*, Phys. Lett. B **728**, 462 (2014).